Methanol Maser Associated Outflows: Detection statistics and properties.

H. M. de Villiers,[1]* A. Chrysostomou[1], M. A. Thompson[1], S. P. Ellingsen[2], J. S. Urquhart[3], S. L. Breen[4], M. G. Burton[5], T. Csengeri[3], D. Ward-Thompson[6]

[1]Centre for Astrophysics Research, University of Hertfordshire, College Lane, Hatfield, Herts, AL10 9AB, United Kingdom
[2]School of Physical Science, University of Tasmania, Private Bag 37, Hobart 7001, TAS, Australia
[3]Max-Planck-Institut für Radioastronomie, Auf dem Hügel 69, D-53121 Bonn, Germany
[4]CSIRO Astronomy and Space Science, Australia Telescope National Facility, PO Box 76, Epping, NSW 1710, Australia
[5]School of Physics, University of New South Wales, Sydney, NSW 2052, Australia
[6]Jeremiah Horrocks Institute, University of Central Lancashire, Preston, Lancashire, PR1 2HE, United Kingdom

24 July 2014

ABSTRACT

We have selected the positions of 54 6.7GHz methanol masers from the Methanol Multibeam Survey catalogue, covering a range of longitudes between 20° and 34° of the Galactic Plane. These positions were mapped in the $J = 3 - 2$ transition of both the ^{13}CO and $C^{18}O$ lines. A total of 58 ^{13}CO emission peaks are found in the vicinity of these maser positions. We search for outflows around all ^{13}CO peaks, and find evidence for high-velocity gas in all cases, spatially resolving the red and blue outflow lobes in 55 cases. Of these sources, 44 have resolved kinematic distances, and are closely associated with the 6.7GHz masers, a sub-set referred to as Methanol Maser Associated Outflows (MMAOs). We calculate the masses of the clumps associated with each peak using 870 μm continuum emission from the ATLASGAL survey. A strong correlation is seen between the clump mass and both outflow mass and mechanical force, lending support to models in which accretion is strongly linked to outflow. We find that the scaling law between outflow activity and clump masses observed for low-mass objects, is also followed by the MMAOs in this study, indicating a commonality in the formation processes of low-mass and high-mass stars.

Key words: line: profiles; masers; molecular data; stars: massive, formation, outflows; submillimetre: stars

1 INTRODUCTION

Massive stars ($> 8M_\odot$) play a key role in the evolution of the Universe, as the principal sources of heavy elements and UV radiation. Their winds, massive outflows, expanding HII regions and supernova explosions serve as an important source of enrichment, mixing and turbulence in the ISM of galaxies (Zinnecker & Yorke, 2007). Our understanding of the formation and evolution of young massive stars is made difficult by their rarity, large average distances that demands observations at higher angular resolution, deeply embedded formation within dense clusters resulting in confusing dynamics and obscuration, and rapid evolution with short-lived evolutionary phases (Shepherd & Churchwell, 1996b; Zinnecker & Yorke, 2007).

The specific formation process of massive stars is not

yet fully understood. These stars reach the zero-age main sequence (ZAMS) while still accreting material from their parent molecular cloud. Due to their high mass, they radiate strongly. This radiation pressure exceeds the gravitational pressure, and should the formation process be similar to low mass stars, the growing radiation pressure from the newborn stars will eventually become strong enough to stop the accretion, yielding an upper mass limit of $\sim 40M_\odot$ (Wolfire & Cassinelli, 1987; Stahler & Palla, 1993).

Previously, two solutions were proposed to overcome this problem: (i) a formation process involving multiple lower mass stars, either via coalescence of low- to intermediate-mass protostars (e.g. Bonnell et al., 1998; Bally & Zinnecker, 2005), or competitive accretion in a clustered environment (e.g. Bonnell et al., 2004), or (ii) a scaled-up version of the process found in low-mass star formation. The latter solution can be sub-divided into the following main categories: (a) increased spherical accretion rates in turbu-

* Email: lientjiedv@gmail.com

lent cloud cores (order $10^{-4} - 10^{-3} M_\odot yr^{-1}$), high enough to overcome the star's radiation pressure (e.g. McKee & Tan, 2003; Norberg & Maeder, 2000) or (b) accretion via disks onto a single massive star (e.g. Jijina & Adams, 1996; Yorke & Sonnhalter, 2002).

A solution to overcome the radiation pressure barrier was proposed by Yorke & Sonnhalter (2002), that involved the generation of a strong anisotropic radiation field where an accretion disk reduces the effects of radiative pressure, by allowing photons to escape along the polar axis (the "flashlight effect"). However, these simulations showed an early end of the disk accretion phase, with final masses limited to $\sim 42 M_\odot$. Krumholz et al. (2009) suggested that the early end of the accretion phase is because the disk loses its shielding property as it cannot be fed in an axially symmetric configuration. Contrary to the stable radiation pressure-driven outflows in Yorke & Sonnhalter (2002), they proposed a three-dimensional radiation hydrodynamic simulation with a Rayleigh-Taylor instability in the outflow region, allowing further accretion onto the disk.

Kuiper et al. (2010) took this further by introducing a dust sublimation front to their simulations. This preserves the shielding of the massive accretion disk and allows the protostar to grow to $\sim 140 M_\odot$.

The easiest way to verify the disk accretion models, would be with the detection of accretion disks around massive protostars, but this is difficult without specialized techniques (e.g. Pestalozzi et al., 2009), because they are small (at most several hundred AU), short lived, and easily confused by envelopes (Kim & Kurtz, 2006). Few clear examples of such disks exist (e.g. Cesaroni et al., 2007; Zapata et al., 2010).

However, we expect that if massive stars do form via accretion disks, they will generate massive and powerful outflows, similar to low-mass stars. These outflows are necessary to transport angular momentum away from a forming star (Shu et al., 1991, 2000; Konigl & Pudritz, 2000; Chrysostomou et al., 2008). For massive stars, these outflows should be of much larger scale and easier to detect than the accretion disks (Kim & Kurtz, 2006). Studying outflows offers an alternative approach to probe the embedded core.

There have been many studies that collectively suggest outflows are ubiquitously associated with massive star formation (e.g. Molinari et al., 1998; Beuther et al., 2002b; Shepherd & Churchwell, 1996a; Xu et al., 2006).

Zhang et al. (2005) found outflow masses (~ 10 to 100's $M_\odot$), momenta (10-100 $M_\odot kms^{-1}$) and energies ($\sim 10^{39}$ J) toward their sample of luminous IRAS point sources about a factor 10 higher than the values of low-mass outflows (Bontemps et al., 1996). This suggests that outflows consist of accelerated gas that has been driven by a young accreting protostar, rather than swept-up ambient material (Churchwell, 1999). It could also be material that originates from the accretion disk / young stellar object and is funnelled out of the central system (e.g Shepherd & Churchwell, 1996a).

To date, CO observations of molecular outflows have been made using mainly two methods: (1) single-point CO line surveys toward samples of massive young stellar objects (YSO's) in search of high-velocity molecular gas (e.g. Shepherd & Churchwell, 1996b; Sridharan et al., 2002) or (2) CO line mapping of carefully selected sources that exhibit high-velocity wings (e.g. Shepherd & Churchwell, 1996a; Beuther

et al., 2002b). Unless outflows are mapped, it is difficult to determine their physical properties. Mapping outflows at sufficient sensitivity and high angular resolution is time-consuming, but the development of heterodyne focal plane arrays (e.g. HARP on JCMT or HERA on IRAM) has made it possible to map statistically significant samples of massive star-forming regions to search for outflows (e.g. Gottschalk et al., 2012; López-Sepulcre et al., 2009).

Outflows are one of the earliest observable signatures of star formation, and are believed to develop from the central objects during the infrared bright stage called the "hot core" phase (Cesaroni et al., 1992; Kurtz et al., 2000), just before the UCHII phase (Shepherd & Churchwell, 1996a; Wu et al., 1999; Molinari et al., 2002; Beuther et al., 2002b; Zhang et al., 2001).

Another important signpost of the "hot core" phase, is the turn-on of radiatively pumped 6.7GHz (class II) methanol masers, the second brightest masers in the Galaxy (Sobolev et al., 1997; Minier et al., 2003; Menten, 1991). Observations indicate that these masers are rarely associated with HII regions, but most of them are found to be associated with massive millimeter and submillimeter sources (e.g. Walsh et al., 2003; Beuther et al., 2002b; Urquhart et al., 2013a). It appears as if these masers occupy a brief phase in the pre-UCHII region, even as short as $\sim 10^4$ years, and disappear as the UCHII region evolves (Hatchell et al., 1998; Codella & Moscadelli, 2000; Codella et al., 2004; van der Walt, 2005; Wu et al., 2010). They are also known to be mostly associated with massive star formation, making them important signposts of massive star formation (Minier et al., 2005; Ellingsen, 2006; Caswell, 2013; Breen et al., 2013).

However, there are limited simultaneous studies of methanol masers and outflow activity. Minier et al. (2001) found that ten out of thirteen absolute positions for class II methanol maser sites coincided with typical tracers of massive star formation (e.g. UCHII regions, outflows and hot cores), while seven out of these ten were within less than 2000 AU ($\sim 10^{-2}$ pc) from outflows. Their results supported the expected association between the occurrence of class II methanol masers and molecular outflows.

The *Spitzer* GLIMPSE survey (Churchwell et al., 2009) revealed a new signpost for outflows in high-mass star formation regions in the form of extended emission which is bright in the 4.5-μm band. These objects are generally referred to either as extended green objects (EGOs) (Cyganowski et al., 2008) or green fuzzies (Chambers et al., 2009). The enhanced emission in this wavelength range is believed to be due to shock-excited H_2 and/or CO band-head emission (De Buizer & Vacca, 2010). Cyganowski et al. (2008) found that many EGOs are associated with 6.7GHz methanol masers, while Chen et al. (2009) showed a high rate of association with shock-excited class I methanol masers at 44 and 95 GHz. Sensitive, high resolution searches for class II methanol masers towards a small sample of EGOs achieved a detection rates of 64% (although this should be considered an upper limit since most targets had known 6.7GHz methanol masers in their vicinity), with approximately 90% of these sources also having associated 44GHz class I methanol maser emission (Cyganowski et al., 2009). These results demonstrate a close association between methanol masers and young high-mass stars with active outflows.

Molecular outflows are more visible than the YSO or

its disk, and because of the association of 6.7GHz methanol masers with massive star formation, searching for outflows toward these masers and studying their physical properties can reveal information regarding the obscured massive cores they are associated with. Moreover, by selecting outflows that are only associated with methanol masers, deliberately biases the resulting sample towards a narrower, relatively well-defined evolutionary range which allows constraints to be placed on the "switch-on" of the outflows and the study of their temporal development. In this paper we focus on the study of the physical properties of the outflows and the relationship of these properties with those of their embedding clumps. In a following publication (de Villiers et al 2014b, in prep.) we will explore the effects of the maser selection bias in our sample and the resulting behaviour in the dynamical ages of our maser selected sample.

We present a survey of ^{13}CO$(J = 3 - 2)$ outflows toward a sample of 6.7GHz Methanol Multibeam (MMB) masers (Breen et al. 2014 in prep., Green et al., 2009) using the HARP instrument on the JCMT. Observations and data reduction are described in §2. In §3 we describe the extraction and analysis of the spectra, as well as outflow mapping and outflow detection frequency. The results are presented in §4, where we demonstrate the calculation of the outflows' physical properties and associated clump masses. The relation between the outflow and associated clump properties are examined, and compared with some low-mass relations found in the literature. We also inspect the correlation between outflow and 6.7GHz maser luminosities, as well as between maser luminosity and clump masses, as a probe of the relationship between the physical properties of the driving force, outflow and associated maser. The main results are summarized in §6.

Although the study of the properties of massive molecular outflows and their relation with associated clump masses is not novel *per se*, the selection of the sources in this study is unique in terms of association with 6.7GHz masers. This allows the selection of sources within a relatively well defined evolutionary phase, which potentially could limit the scatter in parameter space compared to previous work. In this paper, we discuss and investigate the physical properties of the Methanol Maser Associated Outflows (MMAOs), and put them in context with other studies. In a second forthcoming paper, we discuss the effect and implications of the 6.7GHz maser bias of our sample on our results.

2 OBSERVATIONS AND DATA REDUCTION

A sample of 6.7GHz methanol masers were drawn from a preliminary catalogue of Northern Hemisphere masers from the Methanol Multibeam (MMB) Survey which has sub-arcsec positional accuracies (Green et al., 2009). The properties of these masers are described fully in Breen et al. (2014 in prep.). The initial sample selection was chosen to have an even spread in maser luminosity, distance, association with UCHII regions and IR sources. A sample of 70 sources were observed between $20° < l < 34°$.

The targets were observed with the JCMT, on the summit of Mauna Kea, Hawaii on seven nights between 17 May 2007 and 22 July 2008. Targets were mapped in the ^{13}CO and C^{18}O$(J = 3 - 2)$ transitions (330.6 GHz and 329.3
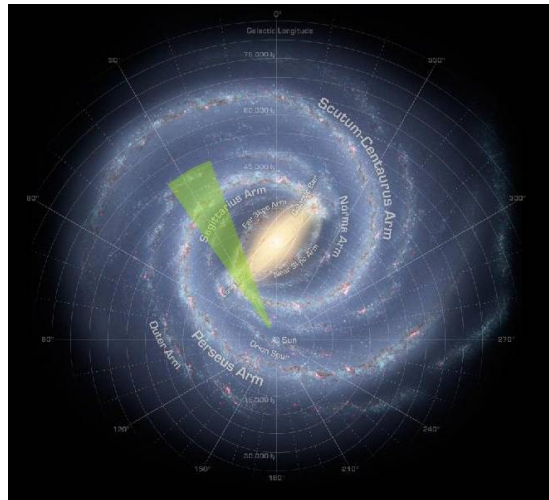

Figure 1. The shaded triangle indicates the approximate area from where the 6.7GHz methanol maser sample were selected for this study. The background sketch is by R. Hurt and R. Benjamin (Churchwell et al., 2009), and shows how the Galaxy is likely to appear face-on, based on radio, infrared and optical data.

GHz), using the 16-receptor Heterodyne Array Receiver Program (HARP). Only 14 of the 16 receptors were operational at the time of observation. The receptors are laid out in a 4×4 grid separated by $30''$ and the beam size of the individual receptors at 345 GHz is $14''$. All the data were corrected for a main-beam efficiency of $\eta_{\mathrm{mb}} = 0.66$ (Smith et al., 2008; Buckle et al., 2009). A HARP jiggle map (Buckle et al., 2009) produces a fully sampled, 16-point rectangular map with a pixel scale of $6''$ and a spectral resolution of 0.06 kms^{-1}. The field-of-view is approximately $2' \times 2'$. As the typical distance to the methanol maser target sources is > 2kpc, and with an estimated maser lifetime of $2.5 - 4 \times 10^4$ years (van der Walt, 2005), the expected outflows from the maser-associated YSOs should be sampled in a single JCMT HARP jiggle-map. The pointing accuracy of the JCMT is of order $2''$ or better. Pointing checks were carried out regularly during observation runs to ensure and maintain accuracy.

The weather during the observations was mostly in JCMT-defined band 3, which implies a sky zenith opacity τ_{225} varying between 0.08 and 0.12 at 225 GHz as measured by the Caltech Submillimeter Observatory tipping radiometer [1].

Out of the 70 observed maser coordinates, 16 observations did not meet one or more of the quality thresholds due to (a) too low signal-to-noise (less than ~ 2), (b) non-functioning receptors (report unreliable temperatures), or (c) target positioning too close to the field-of-view border or a dead receptor. The remaining 54 target coordinates are listed in Table 1 and occur in the shaded area in Figure 1.

The ^{13}CO and C^{18}O maps were simultaneously obtained using the multiple sub-band mode of the back-end Auto-Correlation Spectral Imaging System (ACSIS) (Dent et al., 2000). The raw ACSIS data are in a HARP time series cube, giving the response of the receptors (x-axis) as a function of time (y-axis). The third di-

---

[1] http://www.jach.hawaii.edu/weather/opacity/mk/

mension is the velocity spectrum recorded at the time for that receptor. Data were reduced with the Starlink ORAC-DR pipeline (Cavanagh et al., 2008) using the REDUCE_SCIENCE_NARROWLINE recipe with minor modifications tailored for this dataset[2]. The pipeline reduction process automatically fits and subtracts polynomial baselines. This was followed by truncation of the noisy spectral endpoints, removal of interference spikes and rebinning of the spectrum to a resolution of 0.5 kms^{-1}. Any receptors with high baseline variations compared to the bulk of the spectra, were flagged as bad in addition to those masked out by the pipeline. Lastly the time series were then mapped onto a position-position-velocity (ppv) cube. The reduced data antenna temperature (T_A) had an average RMS noise level of 0.24 K (per 6" × 6" × 0.5 kms^{-1} pixel), or a main-beam efficiency corrected average RMS noise level of $T_{\mathrm{mb}} = 0.36$ K.

[2] http://www.oracdr.org

Table 1. Complete list of 6.7GHz methanol maser coordinates used as pointing targets, including target names. Suffixes "A" and "B" indicate separate clumps if more than one are detected. The clump coordinates from where spectra were extracted are listed. Sources marked with * had their spectra extracted at the maser coordinate itself. The last column lists the noise RMS, integrated over the number of channels n_{chan} in each $C^{18}O$ integrated map ($\phi = \sigma_{RMS}\Delta v \sqrt{n_{chan}}$, for a channel width Δv of 0.5 kms^{-1}). When clumps were truncated at the edge of a map, or signal-to-noise was too low for significant $C^{18}O$ detection, it is indicated.

Target name	Maser coord.		Clump coord.		ϕ
	$l(°)$	$b(°)$	$l(°)$	$b(°)$	K kms^{-1}
G 20.081-0.135	20.081	-0.135	20.081	-0.135	1.1
G 21.882+0.013	21.882	0.013	21.875	0.008	0.9
G 22.038+0.222	22.038	0.222	22.040	0.223	1.7
G 22.356+0.066	22.356	0.066	22.356	0.068	2.0
G 22.435-0.169	22.435	-0.169	22.435	-0.169	1.3
G 23.003+0.124	23.003	0.124	23.002	0.126	1.1
G 23.010-0.411	23.010	-0.411	23.008	-0.410	2.0
G 23.206-0.378	23.206	-0.378	23.209	-0.378	1.0
G 23.365-0.291	23.365	-0.291	23.364	-0.291	1.1
G 23.437-0.184	23.437	-0.184	23.436	-0.183	1.4
G 23.484+0.097	23.484	0.097	23.483	0.098	0.9
G 23.706-0.198	23.706	-0.198	23.706	-0.197	1.3
G 24.329+0.144	24.329	0.144	24.330	0.145	1.4
G 24.493-0.039	24.493	-0.039	24.493	-0.039	1.4
G 24.790+0.083A	24.790	0.083	24.790	0.083	1.6
G 24.790+0.083B	24.790	0.083	24.799	0.097	cut off
G 24.850+0.087	24.850	0.087	24.853	0.085	0.9
G 25.650+1.050	25.650	1.050	25.649	1.051	1.2
G 25.710+0.044	25.710	0.044	25.719	0.051	1.0
G 25.826-0.178	25.826	-0.178	25.824	-0.179	1.2
G 28.148-0.004	28.148	-0.004	28.148	-0.004	0.8
G 28.201-0.049	28.201	-0.049	28.201	-0.049	1.0
G 28.282-0.359	28.282	-0.359	28.289	-0.365	0.6
G 28.305-0.387	28.305	-0.387	28.307	-0.387	0.8
G 28.321-0.011	28.321	-0.011	28.321	-0.011	0.8
G 28.608+0.018	28.608	0.018	28.608	0.018	0.7
G 28.832-0.253	28.832	-0.253	28.832	-0.253	1.3
G 29.603-0.625	29.603	-0.625	29.600	-0.618	1.1
G 29.865-0.043	29.865	-0.043	29.863	-0.045	1.6
G 29.956-0.016A	29.956	-0.016	29.956	-0.017	1.6
G 29.956-0.016B	29.956	-0.016	29.962	-0.008	1.6
G 29.979-0.047	29.979	-0.047	29.979	-0.048	1.7
G 30.317+0.070*	30.317	0.070	30.317	0.070	1.0
G 30.370+0.482A	30.370	0.482	30.370	0.484	0.6
G 30.370+0.482B	30.370	0.482	30.357	0.487	low S/N
G 30.400-0.296	30.400	-0.296	30.403	-0.296	0.8
G 30.419-0.232	30.419	-0.232	30.420	-0.233	1.1
G 30.424+0.466	30.424	0.466	30.424	0.464	0.5
G 30.704-0.068	30.704	-0.068	30.701	-0.067	1.2
G 30.781+0.231	30.781	0.231	30.780	0.231	1.2
G 30.788+0.204	30.788	0.204	30.789	0.205	1.4
G 30.819+0.273	30.819	0.273	30.818	0.273	1.2
G 30.851+0.123	30.851	0.123	30.865	0.114	1.2
G 30.898+0.162	30.898	0.162	30.899	0.163	1.0
G 30.973+0.562	30.973	0.562	30.972	0.561	1.2
G 30.980+0.216	30.980	0.216	30.979	0.216	1.3
G 31.061+0.094	31.061	0.094	31.060	0.092	0.9
G 31.076+0.457	31.076	0.457	31.085	0.468	1.1
G 31.122+0.063	31.122	0.063	31.124	0.063	1.0
G 31.182-0.148A*	31.182	-0.148	31.182	-0.148	1.2
G 31.182-0.148B	31.182	-0.148	31.173	-0.146	cut off
G 31.282+0.062	31.282	0.062	31.281	0.063	0.9
G 31.412+0.307	31.412	0.307	31.412	0.306	1.0
G 31.594-0.192	31.594	-0.192	31.593	-0.193	1.2
G 32.744-0.075	32.744	-0.075	32.746	-0.076	1.1
G 33.317-0.360*	33.317	-0.360	33.317	-0.360	low S/N
G 33.486+0.040*	33.486	0.040	33.486	0.040	low S/N
G 33.634-0.021	33.634	-0.021	33.649	-0.024	1.4

3 DATA ANALYSIS

3.1 Finding the peak emission

^{13}CO was used as an outflow tracer in this study. It is a useful probe of the cloud structure and kinematics, because it traces the higher velocity gas, but has a lower abundance than ^{12}CO, and hence is less contaminated by other high velocity structures within the star forming complex (Arce et al., 2010). Emission from the (J = 3 − 2) transition was observed (T_{trans} = 31.8 K, Curtis et al. (2010)), which traces the warm, dense gas, close to the embedded YSO and also serves as a clearer tracer of warm outflow emission than lower J transitions. Targets were simultaneously observed in the optically thin C^{18}O transition, which serves as a useful tracer of the column density. The C^{18}O emission peak is most likely to coincide with the YSO core's position.

Visual inspection indicated that the positions of peak emission in both ^{13}CO and C^{18}O did not always coincide with the maser coordinate. These offsets were larger than a beam size ($14''$) for seven maser coordinates, with a maximum offset of $1'$. Although it is known that 6.7GHz methanol masers are mostly associated with massive YSOs, two competing and unresolved formation hypotheses state that either methanol masers are embedded in circumstellar tori or accretion disks around the massive protostars (Pestalozzi et al., 2009), or that they generally trace outflows (De Buizer et al., 2012). It thus seems possible that although the masers are in the close vicinity of the YSO, some could be offset, as was found in this study.

Since the peak ^{13}CO emission did not always coincide with the maser coordinates, and the exact coordinate of the peak emission was needed as the position from where the one dimensional spectrum would be extracted as part of the outflow detection method, an alternative method was needed to pin-point this position. *ClumpFind* (Williams et al., 1994), also used by Moore et al. (2007); Buckle et al. (2010); Parsons et al. (2012) was used to carry out a consistent search for the position of peak emission in this study. The search was undertaken on two dimensional images, intensity integrated over the emission peaks' velocity ranges.

In a few cases *ClumpFind* reported more than one clump coordinate per image, likely due to the irregular structure and crowded environment of massive star-forming regions. The purpose of using *ClumpFind* in this study was to find the position of the peak molecular emission in the vicinity of each methanol maser target. Multiple clumps were accepted if they were further than a beam width apart and not close to the edges of the image. Multiple spectra per field-of-view were extracted at these positions. In four cases (marked with asterisk in Table 1) *ClumpFind* did not detect any clumps, either due to low signal-to-noise or the physical area of the emission being too small to satisfy the *ClumpFind* criteria (minimum seven pixels). In these cases we did detect some emission at the maser coordinate, hence we used the maser coordinates as the location for spectrum extraction.

Where clumps were detected close to a dead receptor or the edge of the map, they were rejected from further analysis, as any extracted spectra and derived results will be incomplete. This is the case for the maps of the targets associated with masers G 24.790+0.083 (clump 2), G 30.851+0.123 and G 31.182-0.148 (clump 2).

Of the original 70 targets observed, reliable clump detections were obtained in 54 maps (77%), and because more than one clump was found in some images, a total of 58 positions were analysed. The positions of the observed clumps are summarized in Table 1. Intensity integrated spatial maps were created for these targets, and are shown online in Appendix A, where the integrated C^{18}O emission is contoured over the background of ^{13}CO emission, the latter integrated over velocity ranges v_{low} to v_{high}, listed in Table 2.

Contour intervals are shown in steps of the integrated noise RMS, ϕ, where $\phi = \sigma_{\text{RMS}}\Delta v\sqrt{n_{\text{chan}}}$, calculated for the same number of channels, n_{chan}, over which the C^{18}O image is integrated, with σ_{RMS} the average RMS per channel and $\Delta v = 0.5$ kms^{-1} the velocity range per channel. All values are listed in Table 1. Where contour intervals are larger than 2ϕ, this is indicated in the figure captions. The lowest level contour was manually selected for each image, because every image has a unique signal-to-noise and background. The lowest contour levels ranged between 3ϕ and 14ϕ. Both maser and clump coordinates are indicated on the maps, shown respectively as a star and circle symbol.

Sometimes, C^{18}O noise levels were excessive due to poor atmospheric transmission, as this line is at the edge of the atmospheric window, which makes it susceptible to small changes in the water vapour column. Targets associated with masers G 30.370+0.482 (clump 2), G 31.182-0.148 (clump 1), G 33.317-0.360 and G 33.486+0.040 did not show sufficiently high signal-to-noise to isolate any clump emission above a $3 \times \phi$ threshold. For these targets, the C^{18}O maps are not shown in Appendix A.

3.2 Spectrum extraction and wing selection

After locating the emission peak, the spectrum was extracted at this position from both the ^{13}CO and C^{18}O cubes. Table 2 lists the maser median velocity taken from the literature, or its associated IRDC velocity if the former was not available (Simon et al., 2006) and literature references of these values, for each target. It also gives the measured peak main-beam efficiency corrected temperatures (T_{mb}) and corresponding velocities for both ^{13}CO and C^{18}O. Sources marked with an asterisk exhibit self absorption dips in their ^{13}CO spectra. For these spectra, a Gaussian was fitted to the shoulders of the absorbed spectrum and the peak of this resultant profile was used as the estimate of peak temperature. The peak from the Gaussian fit showed on average a $\sim 13\%$ increase with respect to the peak T_{mb} of the original, absorbed spectrum, with three extreme cases of a $30\% - 40\%$ increase. Two examples of these sources and their Gaussian fits are shown in Figure 2. Plotted C^{18}O spectra give an indication where the optically thin peak is expected. In the case of the double-peaked target G 23.010-0.411, the values marked with an asterisk in Table 2 represent peak values of fits to the individual peaks. The values of Δv_{b} and Δv_{r} in columns 9 and 10 are the blue and red velocities relative to the peak C^{18}O velocity, measured respectively from each wing extreme, to be discussed in §4.4. The use of Int_{b} and Int_{r} in columns 11 and 12 will be discussed in §3.3.
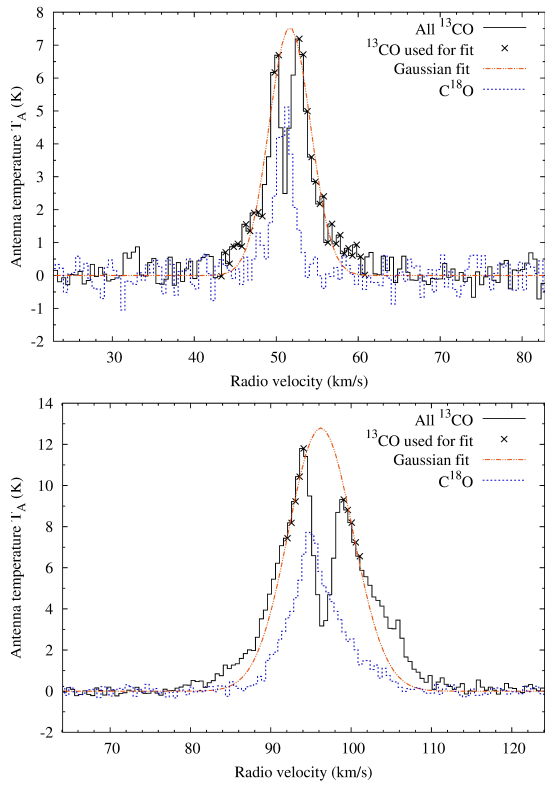
Figure 2. Gaussian fits (dot-dot-dashed lines) to the shoulders of ^{13}CO spectra (crosses) toward G 22.038+0.222 (top) and G 28.201-0.049 (bottom), whose profiles show clear evidence of self absorption. The Gaussian's peak is used as the estimated peak temperature. The C^{18}O spectra (short dashed lines) give an indication where the actual peak is expected.

Table 2. Literature $v_{\rm lsr}$ velocities (median velocity for 6.7GHz maser or associated IRDC or molecular cloud if no maser velocity is available) associated with each target. Observed peak $C^{18}O$ and ^{13}CO $v_{\rm lsr}$ velocities with corresponding temperatures as derived from the each target spectrum's peak antenna temperature at the clump coordinate. These antenna temperatures are corrected for the main-beam efficiency ($\eta = 0.66$). Temperatures marked with * are the peaks of Gaussians fitted to spectrum profiles excluding velocity ranges showing strong self-absorption in ^{13}CO, while for double-peaked G 23.010-0.411, they represent fits to the individual peaks (peak 1 indicated by "(pk.1)" and peak 2 by "(pk.2)"). The velocities over which the ^{13}CO profile is integrated to obtain the background emission shown in Appendixes A and B, are chosen to include all emission and are given by $v_{\rm low}$ and $v_{\rm high}$. Where maximum integrated intensities $Int_{\rm b}$ and $Int_{\rm r}$ are available for respectively blue and red ^{13}CO integrated maps (corrected for main-beam efficiency), they are listed. For monopolar outflows, only one value is given. These intensities are used to determine contour intervals in Appendix B, published online. $\Delta v_{\rm b}$ and $\Delta v_{\rm r}$ are used in §4.4, equations 3, 4 and 7. These are the velocity extents measured from the peak velocity (as defined by $C^{18}O$) to the maximum velocity along the blue or red ^{13}CO line wing (as defined in the text).

Target	Maser v (km s^{-1})	Vel. Ref.	$C^{18}O$ v_p (km s^{-1})	$C^{18}O$ $T_{\rm mb}$ (K)	^{13}CO v_p (km s^{-1})	^{13}CO $T_{\rm mb}$ (K)	($v_{\rm low} \rightarrow v_{\rm high}$) (km s^{-1})	$\Delta v_{\rm b}$ (km s^{-1})	$\Delta v_{\rm r}$ (km s^{-1})	$Int_{\rm b}$ (K km s^{-1})	$Int_{\rm r}$ (K km s^{-1})
G 20.081-0.135	43.8^m	1	41.6	9.1	42.3	14.4*	(20 → 60)	11.1	10.9	35.0	48.4
G 21.882+0.013	20.7^m	1	20.2	4.0	19.8	11.3	(10 → 35)	4.5	6.5	20.3	9.7
G 22.038+0.222	50.4^m	1	51.5	7.8	51.7	11.5*	(40 → 70)	9.3	8.7	20.8	35.8
G 22.356+0.066	82.4^m	1	84.2	5.8	84.4	11.5	(75 → 95)	5.0	3.5	13.9	4.3
G 22.435-0.169	31.2^m	1	27.9	3.3	27.8	7.1	(20 → 40)	2.0	4.5	10.6	5.2
G 23.003+0.124^r	-	-	107.4	3.5	108.5	4.7	(102 → 112)	-	4.0	-	7.7
G 23.010-0.411$_{\rm pk.1}$	77.7^m	1	76.4	4.0	75.6	9.2*	(60 → 90)	11.5	11.0	37.7	27.0
G 23.010-0.411$_{\rm pk.2}$	-	-	78.4	3.8	79.6	9.4*	(60 → 90)	-	-	-	-
G 23.206-0.378	80.3^m	1	77.8	4.0	77.6	5.3*	(65 → 95)	12.0	11.5	18.0	18.9
G 23.365-0.291	77.3^c	4	78.3	4.1	77.8	5.9*	(72 → 85)	3.9	4.6	8.2	11.7
G 23.437-0.184	101.5^m	1	100.6	8.0	101.2	12.7	(90 → 115)	14.5	9.0	31.7	46.1
G 23.484+0.097	87.2^m	1	84.2	5.7	84.2	6.7*	(75 → 95)	4.1	7.4	11.1	10.0
G 23.706-0.198	76.8^m	1	69.1	5.4	68.3	8.3	(60 → 80)	3.5	5.5	17.2	13.7
G 24.329+0.144	115.4^m	1	112.7	4.0	112.8	7.9	(105 → 130)	10.0	6.5	15.7	8.0
G 24.493-0.039	114.0^m	1	111.8	6.1	109.8	14.2	(100 → 120)	6.5	7.5	33.7	17.9
G 24.790+0.083A	111.3^m	1	110.5	9.3	111.6	15.8	(100 → 125)	7.0	6.5	15.1	30.9
G 24.790+0.083B	-	-	110.5	6.4	111.1	11.5	(100 → 120)	9.5	9.5		
G 24.850+0.087	52.6^m	1	108.9	7.3	109.0	14.6	(105 → 115)	4.0	4.0	19.2	14.2
G 25.650+1.050	40.6^m	1	42.3	8.7	43.1	18.0*	(35 → 55)	12.5	10.5	32.5	45.3
G 25.710+0.044	96.2^m	1	101.2	4.2	101.3	14.7	(95 → 110)	9.0	2.5	32.7	25.6
G 25.826-0.178	94.7^m	1	93.2	6.5	91.8	10.9	(80 → 105)	8.0	10.0	22.2	13.8
G 28.148-0.004	100.8^m	1	98.7	6.4	99.0	8.0*	(90 → 115)	7.7	5.8	12.7	12.5
G 28.201-0.049	95.9^m	1	94.9	11.7	96.2	19.4*	(78 → 115)	15.6	15.4	62.3	87.1
G 28.282-0.359	41.6^m	1	47.4	10.6	49.1	17.9*	(40 → 55)	9.3	4.7	29.9	35.8
G 28.305-0.387	80.9^c	1	85.6	8.0	85.9	27.5	(78 → 95)	5.5	3.0	37.1	50.3
G 28.321-0.011	99.0^c	4	99.6	5.2	99.8	12.4	(85 → 110)	8.0	4.5	22.7	17.0
G 28.608+0.018	-	-	103.1	9.0	103.8	22.3	(90 → 115)	11.5	7.0	38.1	25.8
G 28.832-0.253	86.1^m	1	87.2	6.1	88.4	10.6	(72 → 110)	8.0	11.0	20.2	35.1
G 29.603-0.625^r	-	-	77.2	4.0	76.9	7.2	(70 → 90)	-	4.0	-	11.0
G 29.865-0.043	-	-	101.8	9.0	101.1	19.6	(90 → 110)	6.5	6.0	67.9	22.5
G 29.956-0.016A	99.9^m	1	97.8	17.6	97.6	31.7	(90 → 110)	10.5	9.0	63.2	38.8
G 29.956-0.016B	99.9^m	1	97.8	5.8	97.6	20.4	(90 → 108)	5.5	9.0	30.8	38.8
G 29.979-0.047	101.7^m	1	101.8	4.3	101.7	8.2*	(85 → 110)	11.1	5.4	40.1	18.2
G 30.317+0.070	42.6^m	1	44.6	2.9	44.1	6.0	(30 → 50)	5.5	4.5	9.7	5.9
G 30.370+0.482A	-	-	17.4	1.4	17.4	6.0	(10 → 28)	2.5	5.5	4.4	7.7
G 30.370+0.482B	-	-	17.9	1.5	17.4	4.6	(10 → 22)	2.0	2.0	2.5	3.6
G 30.400-0.296	101.7^m	3	103.0	3.9	102.7	12.8	(90 → 115)	10.0	5.0	23.8	16.4
G 30.419-0.232	102.8^m	1	104.5	7.7	104.3	17.2	(95 → 110)	5.0	10.0	30.2	41.4
G 30.424+0.466	9.5^m	3	15.5	3.6	15.6	6.8	(10 → 25)	3.5	6.0	7.4	9.1
G 30.704-0.068^b	88.9^m	1	90.1	9.5	88.9	32.1	(80 → 102)	9.0		50.6	-
G 30.781+0.231	49.5^m	1	41.9	3.7	42.3	10.3	(30 → 55)	4.0	2.5	11.2	17.6
G 30.788+0.204	82.8^m	1	81.6	5.4	82.3	8.0*	(70 → 90)	7.3	6.2	17.0	23.5
G 30.819+0.273^r	104.9^m	1	98.1	3.0	98.1	7.8	(90 → 110)	-	5.5	-	10.2
G 30.851+0.123	-	-	39.4	4.8	40.4	15.6	(30 → 50)	6.5	5.5	-	-
G 30.898+0.162^r	104.5^m	1	105.3	4.2	105.8	9.5	(100 → 115)	-	2.5	-	13.0
G 30.973+0.562	-	-	23.4	3.6	23.5	9.2	(10 → 30)	3.0	3.0	23.6	9.8
G 30.980+0.216^r	-	-	107.4	3.2	107.1	7.2	(100 → 120)	-	4.5	-	8.4
G 31.061+0.094	16.2^m	1	19.2	1.9	17.7	13.6	(10 → 25)	4.0	5.0	19.0	1.0
G 31.076+0.457^b	-	-	28.3	1.9	24.5	5.8*	(15 → 30)	5.1		8.8	-
G 31.122+0.063	-	-	41.5	3.6	41.5	10.4	(30 → 50)	6.5	5.5	10.6	16.7
G 31.182-0.148A	-	-	42.6	1.3	42.6	3.5	(35 → 50)	3.5	2.5	7.2	2.4
G 31.182-0.148B	-	-	43.6	1.6	43.1	5.2	(35 → 50)	3.0	2.0	-	-
G 31.282+0.062	108.0^m	1	109.0	7.4	109.0	14.1*	(100 → 120)	7.0	5.0	23.4	19.3
G 31.412+0.307	96.7^m	1	96.4	8.9	97.3	18.5*	(90 → 108)	4.3	6.2	14.4	25.1
G 31.594-0.192	-	-	43.1	2.3	43.1	7.5	(35 → 50)	3.5	2.5	6.7	8.3
G 32.744-0.075	34.8^m	1	37.5	5.4	37.0	10.8	(25 → 50)	7.0	9.0	25.0	22.7
G 33.317-0.360^r	-	-	34.8	2.4	35.8	3.8	(25 → 45)	-	4.0	-	8.4
G 33.486+0.040	-	-	112.0	1.4	112.2	3.2	(106 → 118)	3.5	2.0	2.1	5.4
G 33.634-0.021	105.900^m	2	103.8	5.9	103.5	13.6	(95 → 115)	2.0	7.5	20.3	8.7

First column superscripts: b = blue lobe only, r = red lobe only. Second column superscripts: m = mid-line velocity, p = peak-velocity, c = cloud velocity.
1. Green & McClure-Griffiths (2011), 2. Roman-Duval et al. (2009), 3. Szymczak et al. (2012), 4. Simon et al. (2006)
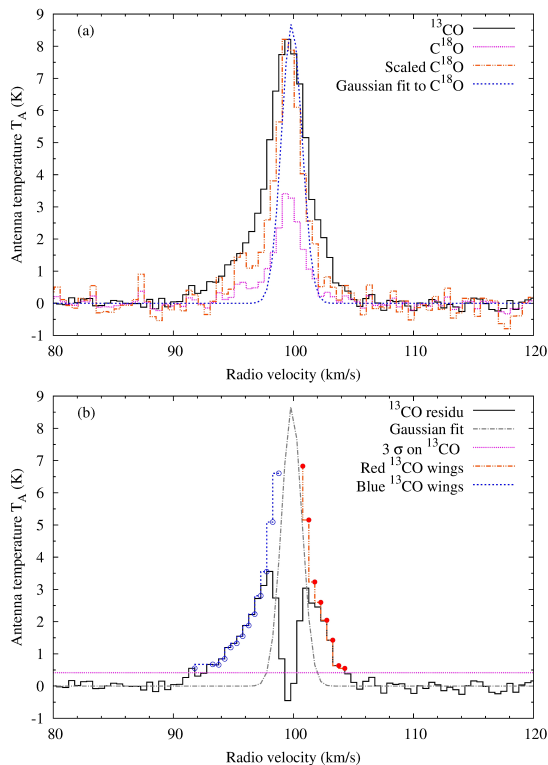
Figure 3. (a) Example of the ^{13}CO spectrum (solid line) for the clump associated with maser G 28.321-0.011. Its C^{18}O spectrum (dot-dashed line) is scaled to the ^{13}CO peak (dot-dot-dashed line) and a Gaussian is fitted to the scaled spectrum (short dashed line). (b) The ^{13}CO residuals following Gaussian subtraction is shown (solid line), along with the 3σ noise level (dotted line) and wing residuals satisfying the selection criteria. Blue wings are indicated by a short dashed line and empty circles, and red wings by a dot-dot-dashed line and solid circles.

Following Codella et al. (2004), the optically thin C^{18}O profiles were used as tracers for the line cores of targets. The C^{18}O spectra were scaled to the ^{13}CO peak temperature. To avoid subtracting any emission from higher velocity features that may be present in the C^{18}O if densities were sufficiently high, a Gaussian was fitted to the C^{18}O peak to approximate the line core-only emission. This was done by gradually removing points from the outer (higher velocity) edges of the C^{18}O spectrum until the peak could be fitted, following the same approach as van der Walt et al. (2007) (see Figure 3 (a)). The scaled Gaussian fit was then subtracted from the ^{13}CO spectra to show the velocity ranges in the line wings where there is excess emission in ^{13}CO.

G 23.010-0.411 is a special case with a double peaked profile. Assuming this is caused by two separate but closely associated clumps, we used two Gaussians, each fitted just to the highest velocity shoulder of each C^{18}O line peak. Whenever absorption dips occur in the ^{13}CO profiles, no natural profile peak existed. Instead, the C^{18}O spectra were scaled to the the peak of the previous Gaussian fitted to the ^{13}CO.

This Gaussian was then subtracted from the ^{13}CO profile. The line wings are defined by the sections where the ^{13}CO profile is broader than the scaled Gaussian representing the C^{18}O line core emission, *provided* the ^{13}CO corrected antenna temperature is higher than 3σ (σ is the noise per

0.5 kms^{-1} channel, averaged over a 30kms^{-1} section of the emission-free spectrum). An example of this wing selection process is shown in Figure 3 (b), which shows the ^{13}CO residual spectrum and discrete spectral points that satisfy the wing criteria (empty circles are blue, and solid circles are red).

There is a risk that some blue and red emission might be missed by analysing a single spectrum at the location of the clump peak. Therefore, when the position of peak intensity in both the blue and red integrated images was found (mapping of blue and red images is explained in §3.3), another two additional spectra, called the "red-wing spectrum" and "blue-wing spectrum", were extracted. Once again blue and red residual spectra were calculated. If broader wing emission was found, the initial wing ranges were expanded to incorporate the ranges covered by the red-wing and blue-wing spectra. The final velocity ranges for blue and red wings are listed in Table 2.

3.3 Mapping the outflows

The final blue- and redshifted velocity ranges are used to produce two dimensional ^{13}CO intensity integrated images corresponding to each wing. These are overlaid as solid blue- and dotted red contours onto the ^{13}CO integrated intensity image, representing the outflow lobes. Two examples are shown in Figure 4, showing target G 24.493-0.039 with the maser and clump coordinates overlapping, and target G 29.956-0.016A with an offset between the maser and clump coordinates. The remainder of the maps are shown online in Appendix B. Contours are plotted in 10% intervals up to 90% of the maximum intensity, $Int_{\rm b}$ or $Int_{\rm r}$, for each integrated image (values listed in columns 10 and 12 in Table 2). The lowest contour is never lower than 30%, but values differ for each image depending on the individual background brightness levels. The lowest contour is selected by eye as the level which encompassed the outflow lobe clearly.

As massive stars form in clusters, the observed targets often have contamination from similarly high velocity components as the outflow, but from different spatial structures in the field of view (Shepherd & Churchwell, 1996a). This makes it difficult to isolate the outflow. Therefore, if identified as belonging to such structures, these pixels were flagged to be bad in any further analysis. Sometimes one or both of the outflows are partially cut-off where they are situated close to the edge of the field-of-view or to a dead receptor. These sources are flagged as such in the second to last column in Table 5 in §4.4 and their calculated properties only serve as a lower limit because a fraction of the emission is not included in the analysis.

Three of the 58 analysed clumps have been too close to the edge of the field of view for any significant information to be derived and are excluded from further analysis. Out of the remaining 55 maps, 47 outflows are clearly bipolar (85%), with the eight exceptions marked with a superscript in Table 2. For a sample of high mass protostellar objects, Beuther et al. (2002b) had a bipolar outflow detection frequency of 81% in ^{12}CO, comparable with what we find.

G24.493 -0.039
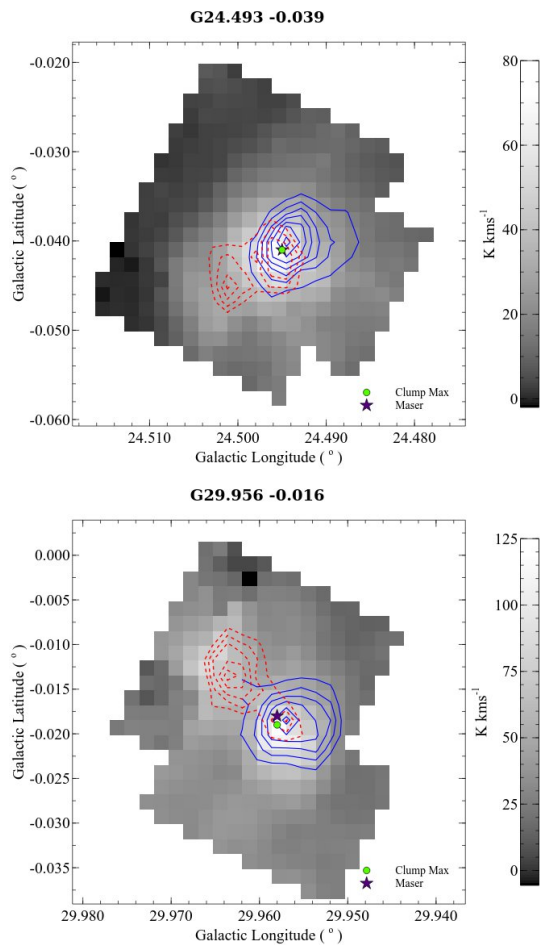

G29.956 -0.016

Figure 4. Two examples of intensity integrated images of the blue and red wing, from top to bottom: G 24.493-0.039 and G 29.956-0.016 (clump 1). Grey scale image shows ^{13}CO, integrated over the peak emission (velocity ranges listed in Table 1), with blue and red contours representing blue and red wing integrated intensities respectively. Contour intervals are 10% of the maximum intensity for each image, increasing up to 90% of the maximum intensity. Lower contours are respectively at 60% and 50% for the two targets.

4   RESULTS

4.1   Detection Frequency

All of the 58 spectra available for analysis (see §3.1) were found to have high velocity outflow signatures, either in the spectra or in the contour maps, resulting in a 100% detection rate. Such a high detection rate of outflows toward massive YSOs is not uncommon. Shepherd & Churchwell (1996b) searched for ^{12}CO(J = 1 − 0) high-velocity line wings toward 122 high-mass star forming regions and detected low-intensity line wings in 94 of them. Of these 94, 90% were associated with high-velocity (HV) gas in the beam. The argument has already been made at that stage, that if the HV gas is due to bipolar outflows, molecular outflows are a common property of newly formed massive stars. Sridharan et al. (2002) detected 84% of sources with high-velocity gas from a ^{12}CO (J = 2 − 1) survey of 69 protostellar candidates.

Zhang et al. (2001,2005) observed a sample of 69 lumi-

nous *IRAS* point sources in CO (J = 2 − 1) and detected 39 molecular outflows toward them (57%). They found the search for outflows hampered for Galactic longitudes < 50° (due to confusion my multiple cloud components when observing in this transition). A total of 39 objects were outside of this region, toward which 35 outflows were detected, resulting in a 90% outflow detection rate.

Kim & Kurtz (2006) observed 12 sources from the same Molinari et al. (1996) catalogue that Zhang et al. (2001) selected their sources from. They detected outflows in 10 sources and adding these sources to the detections from Zhang, results in a detection rate of 88% ([35 + 10 − 3 = 42] out of [39 + 12 − 3 = 48]), taking into account that there are three sources in common between the two samples. More recently, López-Sepulcre et al. (2009) searched for molecular outflows toward a sample of eleven very luminous massive YSOs. They found high-velocity wings, indicative of outflow motions, in 100% of the sample.

Three further studies have dealt specifically with class II methanol masers. Codella et al. (2004) surveyed for molecular outflows towards 136 UCHII regions, out of which 56 positions showed either 6.7GHz methanol or 22.2GHz water maser emission. Their overall outflow detection rate from ^{13}CO(J = 1 − 0) and (J = 2 − 1) transition lines was ∼ 39%, but they found that in cases where observations were made toward 6.7GHz methanol or 22.2GHz water maser emission lines, the outflow detection rate increased to 50%. As their observations were single pointings, they may have missed some outflows that were offset from the masers. Xu et al. (2006) studied molecular outflows using high-resolution CO (J = 1 − 0) mapping toward eight 6.7GHz methanol masers closer than 1.5 kpc. They found outflows in seven of them, an 88% detection rate. Wu et al. (2010) investigated the distinctions between low- and high-luminosity 6.7GHz methanol masers via multi-line mapping observations of various molecular lines, including ^{12}CO(J = 1 − 0), toward a sample of these masers. They found outflows to be common among both sets of masers: of the low-luminosity masers, they found six outflows out of nine, and from the high-luminosity masers they found four outflows out of eight, an over-all detection rate of 59%. Note that the detection frequencies from both Xu et al. (2006) and Wu et al. (2010) are obtained from small number samples.

All these results suggest that the majority of massive YSO's have molecular outflows, and should 6.7GHz methanol masers be present, they are closely associated with the outflow phase.

4.2   Maser distances

Green & McClure-Griffiths (2011) published the kinematic distances for about 50% of the targets in this study, using the 6.7GHz maser mid-velocity as an estimate for the systemic velocity. They used respectively the presence / absence of self-absorption in HI spectra in the proximity of the systemic velocity, to determine whether the source is at the near / far kinematic distance. However, methanol maser emission often consists of a number of strong peaks spread over several kms^{-1}. As differences of only a few kms^{-1} in the velocity of the local standard of rest v_{lsr} can be enough to change the kinematic distance solution from near to far and vice versa in the HI absorption feature method of resolving the former,

using estimated v_{lsr} values form the maser emission could lead to an incorrect distance solution. Therefore, molecular line observations provide more reliable measurements of the clump systemic velocity (Urquhart et al., 2014).

For this reason, and to prevent the additional uncertainties introduced by adopting distances calculated using different techniques by different authors, we decided to recalculate all distances of the methanol masers using their associated $C^{18}O$ peak velocities. This was done using the Galactic Rotation Curve (GRC) as fitted by Brand & Blitz (1993), with the Sun's Galactocentric distance, R_0, assumed as 8.5 kpc and its circular rotation Θ_0 as 220 kms^{-1}. Calculated values are listed in Table 3. The average difference between distances calculated using the GRC, versus the maser distances listed by Green & McClure-Griffiths (2011) for our targets, is 0.8 ± 0.6 kpc.

Alternative solutions to Brand & Blitz (1993) for calculating the kinematic distances, are Reid et al. (e.g. 2009) and Clemens (1985). Urquhart et al. (2014) found that for sources in the inner Galaxy, the distances given respectively by these rotation curves, all agree within a few tenths of a kpc, which are smaller than their associated uncertainty of the order ± 1 kpc due to streaming motions (Urquhart et al., 2011, 2012). Consequently, the statistical results are robust against the choice of model.

The galactocentric distances obtained using the GRC from Brand & Blitz (1993) were geometrically converted to heliocentric distances, of which two solutions exist within the solar circle, called the kinematic distance ambiguity (KDA). These distances are equally spaced on either side of the tangent position, and are generally referred to as the near and far distances. Sources with velocities within 10 kms^{-1} of the tangent velocity are placed at the tangent distance (indicated by TAN in the reference column), since the error in the distance is comparable to the difference between the near/far distance and the tangent distance.

As Green & McClure-Griffiths (2011) could resolve the kinematic distance ambiguity for many masers using corresponding HI self-absorption profiles, when available, we used their values to resolve the KDAs for our targets. Where maser distances were not published in Green & McClure-Griffiths (2011), alternative sources were used where available, being other publications of 6.7GHzmasers (Purcell et al., 2006; Caswell & Green, 2011), EGOs (Cyganowski et al., 2009), OH-masers (Fish et al., 2003), associated IRDCs (Simon et al., 2006), or molecular clouds (Roman-Duval et al., 2009) (if the maser position fell within the cloud as well as within ~ 5 kms^{-1} of the cloud's v_{lsr}) were used to resolve our KDAs. The literature reference used to resolve the distance for each source, should it exist, is also listed in Table 3.

For four out of the 58 targets, no published distance could be found to resolve the KDA. In these cases both the near and far values are listed. Three targets are rejected from this list in Table 3: G 24.790+0.083B, because of too high noise, and G 30.851+0.123 and G 31.182-0.148B, because the clumps are mostly cut off by the edge of the field-of-view. The columns after the distance columns, list outflow lobe surface areas and lengths, values used for calculations discussed in §4.4.

Table 3. Target $C^{18}O$ velocities used to calculate their kinematic distances from the Galactic Rotation Curve (Brand & Blitz, 1993). Literature references used to resolve the far/near distance ambiguities are listed in the fourth column, being an assembly from published 6.7GHz masers, OHmasers, EGOs, IRCD's and molecular clouds. Sources with velocities within 10 kms^{-1} of the tangent velocity are placed at the tangent distance, indicated by TAN. Columns five to eight show information used in §4.4: the surface areas A for blue and red lobes as mapped in ^{13}CO and lobe lengths l as measured from the clump coordinate to each outflow's radial extreme.

Target	$C^{18}O$ v (kms^{-1})	D (kpc)	Literature Reference	A_b (pc^2)	A_r (pc^2)	l_b (pc)	l_r (pc)
G 20.081-0.135	41.602	12.6	Fish et al. (2003)	1.48	1.75	1.28	0.92
G 21.882+0.013	20.158	1.8	Purcell et al. (2006)	0.06	0.05	0.29	0.23
G 22.038+0.222	51.533	3.8	Cyganowski et al. (2009)	0.29	0.29	0.60	0.44
G 22.356+0.066	84.189	5.2	Green & McClure-Griffiths (2011)	0.41	0.62	0.53	1.59
G 22.435-0.169	27.895	13.4	Roman-Duval et al. (2009)	2.27	1.06	1.56	0.78
G 23.003+0.124^r	107.445	6.2	Roman-Duval et al. (2009)	-	0.26	-	0.54
G 23.010-0.411	76.380	4.8	Green & McClure-Griffiths (2011)	1.03	0.68	1.48	0.99
G 23.206-0.378	77.829	10.7	Green & McClure-Griffiths (2011)	0.97	1.17	1.40	1.40
G 23.365-0.291	78.292	4.9	Roman-Duval et al. (2009)	0.35	0.53	1.14	1.07
G 23.437-0.184	100.630	5.9	Green & McClure-Griffiths (2011)	0.52	0.90	0.77	0.85
G 23.484+0.097	84.181	5.2	Simon et al. (2006)	0.50	0.25	0.68	0.53
G 23.706-0.198	69.090	11.1	Green & McClure-Griffiths (2011)	5.07	4.35	2.25	3.06
G 24.329+0.144	112.743	7.7	TAN	0.86	0.81	1.01	0.68
G 24.493-0.039	111.752	6.4	Caswell & Green (2011)	1.19	0.91	1.03	0.94
G 24.790+0.083A	110.548	9.1	Green & McClure-Griffiths (2011)	0.49	0.56	0.92	0.79
G 24.850+0.087	108.941	6.3	Roman-Duval et al. (2009)	0.40	1.48	0.82	1.19
G 25.650+1.050	42.315	12.3	Green & McClure-Griffiths (2011)	4.83	4.58	2.32	1.61
G 25.710+0.044	101.214	9.4	Green & McClure-Griffiths (2011)	1.86	2.83	2.46	1.77
G 25.826-0.178	93.206	5.5	Green & McClure-Griffiths (2011)	0.60	0.26	0.81	0.65
G 28.148-0.004	98.665	5.9	Green & McClure-Griffiths (2011)	0.68	0.59	0.86	0.95
G 28.201-0.049	94.860	9.3	Green & McClure-Griffiths (2011)	1.10	1.75	0.81	1.35
G 28.282-0.359	47.354	3.2	Green & McClure-Griffiths (2011)	0.24	0.44	0.61	0.76
G 28.305-0.387	85.627	9.8	Green & McClure-Griffiths (2011)	2.02	4.44	1.42	1.56
G 28.321-0.011	99.570	6.0	Roman-Duval et al. (2009)	0.94	1.33	0.70	1.04
G 28.608+0.018	103.075	7.5	TAN	0.80	1.23	1.09	1.09
G 28.832-0.253	87.189	5.3	Green & McClure-Griffiths (2011)	1.31	0.48	0.93	0.69
G 29.603-0.625^r	77.185	4.8	Roman-Duval et al. (2009)	-	0.54	-	0.84
G 29.865-0.043	101.849	7.4	TAN	1.79	1.98	2.36	1.61
G 29.956-0.016A	97.838	7.4	TAN	1.51	1.19	1.18	1.61
G 29.956-0.016B	97.838	7.4	TAN	0.55	0.92	0.64	1.18
G 29.979-0.047	101.843	7.4	TAN	0.96	0.87	1.29	0.64
G 30.317+0.070	44.645	11.6	Green & McClure-Griffiths (2011)	1.83	1.49	1.52	1.52
G 30.370+0.482A	17.414	13.4	Roman-Duval et al. (2009)	3.03	1.36	1.95	1.36
G 30.370+0.482B	17.914	13.4	Roman-Duval et al. (2009)	2.58	1.67	2.92	1.17
G 30.400-0.296	102.959	7.3	TAN	1.23	0.77	1.39	0.96
G 30.419-0.232	104.549	7.3	TAN	0.73	1.59	2.00	2.03
G 30.424+0.466	15.493	13.5	Roman-Duval et al. (2009)	4.64	4.95	3.74	2.36
G 30.704-0.068^b	90.123	5.5	Green & McClure-Griffiths (2011)	0.49	-	0.40	-
G 30.781+0.231	41.851	2.9	Green & McClure-Griffiths (2011)	0.13	0.09	0.29	0.25
G 30.788+0.204	81.615	9.5	Green & McClure-Griffiths (2011)	2.55	1.16	1.39	0.83
G 30.819+0.273^r	98.128	6.1	Green & McClure-Griffiths (2011)	-	0.58	-	0.80
G 30.898+0.162^r	105.328	7.3	TAN	-	0.86	-	1.49
G 30.973+0.562	23.396	12.89, 1.7	-	4.64, 0.08	2.25, 0.04	1.69, 0.22	1.12, 0.15
G 30.980+0.216^r	107.365	7.3	Roman-Duval et al. (2009)	-	1.12	-	1.06
G 31.061+0.094	19.227	13.2, 1.4	-	2.05, 0.02	0.29, 0.003	1.53, 0.16	0.96, 0.10
G 31.076+0.457^b	28.310	12.5, 2.0	-	4.26, 0.11	3.59, 0.09	3.10, 0.50	
G 31.122+0.063	41.528	11.7	Roman-Duval et al. (2009)	5.11	3.25	3.58	3.58
G 31.182-0.148A	42.648	11.6	Roman-Duval et al. (2009)	2.30	1.26	1.02	0.85
G 31.282+0.062	109.028	7.3	TAN	1.61	1.16	1.58	1.27
G 31.412+0.307	96.428	7.3	TAN	0.58	1.42	0.63	0.84
G 31.594-0.192	43.149	11.6	Roman-Duval et al. (2009)	3.17	5.09	1.18	3.70
G 32.744-0.075	37.528	11.7	Green & McClure-Griffiths (2011)	2.10	2.21	1.54	1.19
G 33.317-0.360^r	34.814	11.8, 2.4	-	-	2.13, 0.09	-	1.38, 0.28
G 33.486+0.040	111.986	7.1	TAN	0.17	0.64	0.52	1.13
G 33.634-0.021	103.750	7.1	TAN	0.93	0.42	0.72	0.62

4.3 Dealing with uncertainties

Calculation of the physical properties of molecular outflows can provide useful information on the obscured driving source. These calculations are subject to a number of uncertainties, most prominent of which is the outflow orientation. However, this is not easily determined (e.g. Shepherd & Churchwell, 1996b; Curtis et al., 2010) and, as such, no correction is applied in this study. Although we will not apply any corrections, we discuss in the following paragraphs the corrections usually applied in the literature for outflow orientation. We also report the effects of such corrections on the calculated outflow properties, as well as additional contributors to uncertainties.

Our observations were some of the first to be carried out with the HARP instrument and some of the receptors exhibited poor performance and did not yield useful data. Often more than two receptors had to be switched off. At times this resulted in some of the clump / outflow emission being missed. Potentially, this could also result in outflow lobes not being detected at all. Blue and red contour levels were determined by eye, since each image is uniquely characterised by the background noise, emission brightness and available receptors. The $14''$ beam of the telescope places a limit on the size of outflows that can be resolved, especially for the more distant targets.

The most significant of the above uncertainties, is θ, the angle of the outflow axis with respect to the line of sight. As only a projection of the outflow is observed, any inclination with respect to the plane of sky will reduce the length of the outflow (not the width) by $\sin(\theta)$, and increase the observed Doppler broadening by $\cos(\theta)$. Cabrit & Bertout (1990) give a detailed discussion of the effect of inclination angle. Due to the lack of a specific orientation for each outflow, many authors assume a mean inclination angle for their sample to correct the calculated outflow parameters. The most commonly used angle is 57.3^o, determined using the assumption that outflows are distributed uniformly and with random inclinations to the line of sight (Bontemps et al., 1996; Beuther et al., 2002b; Hatchell et al., 2007; Curtis et al., 2010). Table 4 summarises the corrections due to inclination for the outflow parameters calculated (see §4.4). Unknown inclinations mostly cause the outflow parameters to be under-estimated. Timescales t_d are thus likely to represent a lower limit to the true age of the outflows (Parker et al., 1991) and hence also to the time over which the embedded proto-stars responsible for the outflows have been accreting from their surroundings (Beuther et al., 2002b).

Other contributors to uncertainties are: possible difficulty separating the outflowing gas from the ambient gas; higher interstellar extinction toward the molecular ring in the inner Galaxy ($0^o < l < 50^o$) in addition to their internal extinction (Zhang et al., 2005); different CO/H_2 abundance ratios used by different authors (e.g. Rodriguez et al., 1982; Cabrit & Bertout, 1992; Herbst & van Dishoeck, 2009).

Some authors use the mean atomic weight of the mixture of hydrogen and helium gas (Garden et al., 1991), while others only consider pure hydrogen molecular gas (Snell et al., 1984), resulting in a difference of 0.36 amu in the mean atomic weight (Wu et al., 2004). The excitation temperature, T_{ex}, is assumed to range from 30 to 50 K for high mass sources (Shepherd & Churchwell, 1996b; Beuther

Table 4. Inclination angle corrections on outflow parameters. All values in column 3 calculated for $\theta = 57.3^\circ$.

Flow parameters	Correction	Corr. Val.	Lit. Val.
p	$1/\cos(\theta)$	1.9	$2^{1,2,3}$
E_m	$1/\cos^2(\theta)$	3.4	$3^{1,2,3}$
t_d	$\cot(\theta)$	0.6	$*^4$
$\dot{M}_{out}$	$\tan(\theta)$	1.6	
F_m	$\sin(\theta)/\cos^2(\theta)$	2.9	$3^{5,6}$
L_m	$\sin(\theta)/\cos^3(\theta)$	5.3	

*for $20^o < \theta < 70^o$, 0.4 to 2.7
1.Wu et al. (2004), 2.Goldsmith et al. (1984),
3.Curtis et al. (2010),4.Zhang et al. (2005),
5.Henning et al. (2000), 6.Beuther et al. (2002b)

et al., 2002b; Wu et al., 2004). However, a constant temperature assumption will underestimate the kinetic energy for an outflow with high jet/ambient density contrast (Downes & Cabrit, 2007). Contamination from additional unrelated velocity components within the telescope beam could make it difficult to isolate the outflow, unless the components have a different spatial distribution from the outflow gas (Shepherd & Churchwell, 1996a). Finally, even though we used ^{13}CO as a tracer, we note that for their ^{12}CO observations, Cabrit & Bertout (1990) estimated typical errors in the outflow parameters that reflect uncertainties in $^{12}CO/H_2$, distance determinations, T_{ex}, inclination angles, optical depth effects and possible low-level contamination of ^{12}CO emission in the reference position. These error values are a factor ~ 3 on outflow mass M_{out}, a factor ~ 10 on mechanical force F_m, and a factor ~ 30 on mechanical luminosity L_m.

4.4 Calculation of outflow physical properties

The physical properties of the outflows are calculated following Beuther et al. (2002b), with some adaptions given that ^{13}CO was observed instead of ^{12}CO. We refer to Curtis et al. (2010) for the derivation of H_2 column density from ^{13}CO. It is assumed that ^{13}CO line wings are optically thin. The column density of ^{13}CO is given by

$$N(^{13}CO) = 5 \times 10^{12} T_{ex} \exp\left(\frac{T_{trans}}{T_{ex}}\right) \int T_{mb} dv \, cm^{-2}, \quad (1)$$

with $T_{trans} = 31.8$ K, the upper level energy of the $J = 3 - 2$ transition of ^{13}CO (Minchin et al., 1993). The excitation temperature of the outflow lobes, T_{ex}, is taken as 35 K (e.g. Shepherd & Churchwell, 1996a; Henning et al., 2000; Beuther et al., 2002b). $\int T_{mb} dv$ is the mean integrated emission (main-beam temperature) for the blue and red lobes. It is calculated by averaging the temperature of each lobe within an area defined by the lowest contour.

The abundance ratio $[H_2]/[^{13}CO]$ is used to convert to the H_2 column density for each lobe, $N_{r/b}$ (red or blue). The isotopic ratio $[^{12}CO]/[^{13}CO]$ is a function of the Galactocentric distance, D_{gal}, of each source, given by Wilson & Rood (1994) as $7.5 D_{gal} + 7.6$, which is then converted to a $[H_2]/[^{13}CO]$ ratio assuming $[CO]/[H_2] = 10^{-4}$ (Frerking et al., 1982). These column densities are then used to calculate the mass of each lobe:

$$M_{b/r} = \left(N_{b/r} \times A_{b/r}\right) m_{H_2}. \quad (2)$$

$A_{r/b}$ is the surface area of each lobe and m_{H_2} is the mass of a hydrogen molecule. This surface area (listed in Table 3) is calculated using the same threshold technique used to calculate T_{mb}, followed by summing the total number of pixels in each lobe and converting to an area using the target's distance as given in Table 3. Where a significant amount of emission was cut off due to a field-of-view edge or dead receptors, it is indicated in the second to last column of Table 5. In these cases the estimated physical parameters should be regarded as lower limits. Finally, the total mass M_{out} is obtained by adding the blue and red components: $M_{out} = M_b + M_r$. Excluding outflows with distance ambiguities (and hence two possible values for M_{out}), and multiplying monopolar outflow masses with two, to account for the missing lobe, outflow masses ranged from 4.0 $M_\odot$ to 750 $M_\odot$ with a median of 73 $M_\odot$ and a mean of 120 $M_\odot$.

Using the outflow masses and Δv_b and Δv_r, which are the blue and red velocities relative to the peak $C^{18}O$ velocity, measured respectively from each wing extreme (listed in Table 2), Beuther et al. (2002b) calculated the outflow momentum p and energy E using:

$$p = M_b \times \Delta v_b + M_r \times \Delta v_r \qquad (3)$$

$$E = \frac{1}{2} M_b \times \Delta v_b^2 + \frac{1}{2} M_r \times \Delta v_r^2. \qquad (4)$$

However, using the maximum wing velocities is likely to overestimate the momentum and energy of the outflows. Instead we make the more reasonable assumption that the material is moving at the observed velocity associated with it. For each "pixel" in the defined outflow lobe area, we calculate the momentum/energy per velocity channel (width Δv), using the channel velocity relative to the systemic velocity (v_i), and the gas mass (M_i) corresponding to the emission in that channel. This is followed by both summing over all velocity channels, and all pixels in the lobe area $A_{b/r}$.

$$p = \sum_{A_b} \left[\sum_{i=v_b} M_{b_i} v_i \right] \Delta v + \sum_{A_r} \left[\sum_{i=v_r} M_{r_i} v_i \right] \Delta v \qquad (5)$$

A similar approach is followed for energy calculations.

$$E = \frac{1}{2} \sum_{A_b} \left[\sum_{i=v_b} M_{b_i} v_i^2 \right] \Delta v + \frac{1}{2} \sum_{A_r} \left[\sum_{i=v_r} M_{r_i} v_i^2 \right] \Delta v. \qquad (6)$$

^{13}CO is a less abundant molecule than ^{12}CO, thus exhibiting a narrower spectral profile. A sample of 56 sources for which both ^{12}CO and ^{13}CO spectra were published, has been investigated and the average $^{12}CO/^{13}CO$ full width zero intensity ratio is found to be ~ 2 with a standard deviation of 1.3 (Cabrit et al., 1988; Shepherd & Churchwell, 1996a; Su et al., 2004; Bronfman et al., 2008; Narayanan et al., 2012; Ortega et al., 2012; Xu & Wang, 2013). All calculations containing wing velocities relative to the systemic velocity are scaled by this factor, implying a factor two increase in p and factor four increase in E.

In order to calculate the dynamical timescale t_d, the length of each outflow lobe l_b or l_r is measured from the clump coordinate to the furthest radial distance. Excluding sources with distance ambiguities, blue-red averaged lobe lengths varies between 0.3-3.6 pc with a mean of 1.2 pc (Table 3). As the red/blue lobe lengths are often different, the

maximum, l_{max} is chosen and used to calculate t_d as

$$t_d = \frac{l_{max}}{(\Delta v_b + \Delta v_r)/2}. \qquad (7)$$

For monopolar outflow detections (e.g. red lobe only), the above formula is adapted to $t_d = l_r/v_r$.

The mass loss rate of the molecular outflow $\dot{M}_{out}$, the mechanical force F_m and the mechanical luminosity L_m summed over both blue and red lobes for each target, are calculated using

$$\dot{M}_{out} = \frac{M_{out}}{t} \qquad (8)$$

$$F_m = \frac{p}{t} \qquad (9)$$

$$L_m = \frac{E}{t}, \qquad (10)$$

where $^{12}CO/^{13}CO$ scaling will again lead to a factor two increase in F_m and factor four increase in L_m. The results are summarised in Table 5. Peculiarities are indicated in the *notes* column. Monopolar target names are marked with a superscript b or r in Table 5, with the letter indicating which lobe (blue or red) is present.

For sources with unresolved distances, both values are shown and distinguished by the numbers next to the target names (1=far and 2=near). Exclusions are then made in further analyses for targets which have (i) kinematic distance ambiguities, hence uncertainties in calculated physical parameters, or, (ii) offsets of more than 3 pixels (18″, of the order of a beam size) between the maser coordinate and peak CO emission. These targets are marked as such in the notes of Table 5. Following the exclusions, we are left with 44 outflows in our sample that are positionally associated with methanol masers and for which we can calculate physical properties that are unaffected by distance ambiguities. We refer to this sample as Methanol Maser Associated Outflows (MMAOs), indicated as such in Table 5, and base all further discussion on these outflows.

Table 5. Physical properties of all blue and red outflow lobes as detected in ^{13}CO. Where multiple clumps exist, their target labels are distinguished by "A" and "B". Both values are listed for sources with distance ambiguities, with (1) next to the target name indicating values for far distances, and (2) mark the values for near distances. Application of the ^{12}CO/^{13}CO scaling factor to wing velocity ranges will lead to a factor two increase in p and F_m and factor four increase in E and L_m. Column 11 lists any additional notes about the mapped lobes and column 12 indicates whether a target belongs to the Methanol Maser Associated Outflows (MMAOs) subset (as defined in §4.4) or not.

Target	M_b	M_r	M_{out}	p	E	t	$\dot{M}_{out}$	F_m	L_m	Notes	MMAO?
	M$_\odot$	M$_\odot$	M$_\odot$	M$_\odot$kms^{-1}	J	yr	10^{-4}M$_\odot$yr^{-1}	M$_\odot$kms^{-1}yr	L$_\odot$		
G 20.081-0.135	110	180	280	2700	1.5E+41	5.7E+04	50	4.6E-02	210	B/R partly c.o.	Y
G 21.882+0.013	3	1	4	23	8.4E+38	2.6E+04	2	8.9E-04	3	Big offset-X	N
G 22.038+0.222	12	18	30	170	7.3E+39	3.3E+04	9	5.3E-03	18		Y
G 22.356+0.066	10	4	14	70	2.0E+39	1.8E+05	1	3.8E-04	1		Y
G 22.435-0.169	55	16	71	240	5.8E+39	2.3E+05	3	1.0E-03	2		Y
G 23.003+0.124^r	-	3	3	13	3.6E+38	6.6E+04	1	1.9E-04	0	No B	Y
G 23.010-0.411	74	31	100	1200	8.1E+40	6.4E+04	16	1.8E-02	100	2 peaks,1clump	Y
G 23.206-0.378	38	38	76	670	4.0E+40	5.8E+04	13	1.2E-02	57		Y
G 23.365-0.291	7	12	20	83	2.1E+39	1.3E+05	2	6.3E-04	1		Y
G 23.437-0.184	30	81	110	1100	6.6E+40	3.6E+04	31	3.1E-02	150		Y
G 23.484+0.097	10	6	16	82	2.7E+39	5.8E+04	3	1.4E-03	4	B/R partly c.o.	Y
G 23.706-0.198	160	110	270	1100	2.8E+40	3.3E+05	8	3.4E-03	7	R partly c.o.	Y
G 24.329+0.144	24	11	35	230	1.0E+40	6.0E+04	6	3.8E-03	14		Y
G 24.493-0.039	50	31	81	700	3.4E+40	7.2E+04	11	9.8E-03	39		Y
G 24.790+0.083A	17	31	48	400	1.8E+40	6.7E+04	7	6.0E-03	23		Y
G 24.790+0.083B	-	-	-	-	-	-	-	-	-	clump c.o.-X	N
G 24.850+0.087	12	30	42	170	3.6E+39	1.5E+05	3	1.1E-03	2	R partly c.o.	Y
G 25.650+1.050	400	350	750	7600	4.6E+41	9.9E+04	76	7.8E-02	380		Y
G 25.710+0.044	110	110	220	880	2.9E+40	2.1E+05	10	4.2E-03	12	Big offset-X	N
G 25.826-0.178	18	7	25	190	9.2E+39	4.4E+04	6	4.3E-03	17		Y
G 28.148-0.004	14	12	26	140	4.4E+39	6.9E+04	4	2.0E-03	5		Y
G 28.201-0.049	120	250	370	4400	3.4E+41	4.3E+04	86	1.0E-01	660		Y
G 28.282-0.359	16	37	53	340	1.3E+40	5.3E+04	10	6.5E-03	21	Big offset-X, B/R partly c.o.	N
G 28.305-0.387	160	410	570	1700	3.5E+40	1.8E+05	32	9.3E-03	16	R partly c.o.	Y
G 28.321-0.011	34	36	70	280	7.6E+39	8.2E+04	9	3.4E-03	8	R partly c.o.	Y
G 28.608+0.018	63	51	110	920	4.7E+40	5.7E+04	20	1.6E-02	67	B/R partly c.o.	Y
G 28.832-0.253	43	38	81	660	3.8E+40	4.8E+04	17	1.4E-02	66		Y
G 29.603-0.625^r	-	13	13	41	8.1E+38	1.0E+05	3	4.0E-04	1	Big offset-X, no B	N
G 29.865-0.043	240	61	300	1900	6.5E+40	1.8E+05	16	1.0E-02	29	B partly c.o.	Y
G 29.956-0.016A	160	90	250	1800	7.6E+40	8.1E+04	31	2.2E-02	78		Y
G 29.956-0.016B	8	13	21	180	8.4E+39	7.9E+04	3	2.3E-03	9	Big offset-X	N
G 29.979-0.047	93	26	120	1100	6.6E+40	7.6E+04	16	1.4E-02	72		Y
G 30.317+0.070	42	25	67	320	9.1E+39	1.5E+05	5	2.1E-03	5	R partly c.o.	Y
G 30.370+0.482A	43	29	73	310	8.2E+39	2.4E+05	3	1.3E-03	3		Y
G 30.370+0.482B	3	2	5	15	2.5E+38	7.1E+05	0	2.1E-05	0	Big offset-X, B mostly c.o.	N
G 30.400-0.296	65	20	84	500	2.1E+40	9.0E+04	9	5.5E-03	20		Y
G 30.419-0.232	53	140	190	810	2.4E+40	1.3E+05	15	6.1E-03	15	B mostly c.o.	Y
G 30.424+0.466	100	130	230	990	2.4E+40	3.8E+05	6	2.6E-03	5	B/R partly c.o.	Y
G 30.704-0.068^b	67	-	67	200	9.1E+39	2.2E+04	61	9.1E-03	34	RR-X red lobe	Y
G 30.781+0.231	4	4	8	24	4.6E+38	4.4E+04	2	5.5E-04	1		Y
G 30.788+0.204	76	48	120	830	3.3E+40	1.0E+05	12	8.2E-03	27		Y
G 30.819+0.273^r	-	11	11	59	1.9E+39	7.2E+04	3	8.2E-04	2	no B	Y
G 30.851+0.123	-	-	-	-	-	-	-	-	-	clump c.o., Big offset-X	N
G 30.898+0.162^r	-	26	26	170	3.8E+39	2.9E+05	2	5.7E-04	1	no B, RR-adapted shape	Y
G 30.973+0.562(1)	250	58	310	590	9.0E+39	2.7E+05	11	2.1E-03	3		N
G 30.973+0.562(2)	4	1	5	10	1.5E+38	3.6E+04	2	2.8E-04	0		N
G 30.980+0.216^r	-	19	19	850	4.7E+41	1.2E+05	3	7.3E-03	330	B separated-X, partly c.o.	Y
G 31.061+0.094(1)	110	1	110	780	2.9E+40	1.7E+05	7	4.7E-03	15	Sub-resolution R	N
G 31.061+0.094(2)	1	0	1	9	3.3E+38	1.8E+04	1	5.0E-04	2	Sub-resolution R	N
G 31.076+0.457^b(1)	110	-	110	1500	1.1E+41	3.0E+05	7	5.1E-03	30	Big offset-X, RR-X red lobe	N
G 31.076+0.457^b(2)	3	-	12	40	2.8E+39	3.8E+04	6	1.1E-03	6	Big offset-X, RR-X red lobe	N
G 31.122+0.063	170	130	300	2000	7.8E+40	2.9E+05	10	6.9E-03	22	B/R partly c.o.	Y
G 31.182-0.148A	43	7	50	190	4.1E+39	1.7E+05	3	1.2E-03	2		Y
G 31.182-0.148B	-	-	-	-	-	-	-	-	-	clump c.o.-X	N
G 31.282+0.062	73	42	110	810	3.1E+40	1.3E+05	9	6.2E-03	20		Y
G 31.412+0.307	15	58	73	680	3.3E+40	7.9E+04	9	8.6E-03	35		Y
G 31.594-0.192	47	120	160	600	1.2E+40	6.0E+05	3	9.9E-04	2	R partly c.o.	Y
G 32.744-0.075	110	110	220	1700	7.6E+40	9.4E+04	24	1.8E-02	67		Y
G 33.317-0.360^r(1)	-	46	46	240	6.7E+39	1.7E+05	6	1.4E-03	3	no B	N
G 33.317-0.360^r(2)	-	2	2	10	2.7E+38	6.8E+04	1	1.4E-04	0	no B	N
G 33.486+0.040	1	7	8	19	3.1E+38	2.0E+05	0	9.6E-05	0	Sub-resolution B	Y
G 33.634-0.021	37	9	46	110	2.2E+39	7.4E+04	6	1.5E-03	3	Big offset-X, B partly c.o.	N

Notes key: R=red lobe, B=blue lobe; RR=red ridge morphology; Offset=clump-maser coordinate offset; X=reject

4.5 Clump masses

The evolutionary sequence of massive stars begins with prestellar clumps and cores, which are gravitationally bound overdensities inside a molecular cloud that show signs of inward motion before a protostar starts forming (Zinnecker & Yorke, 2007; Dunham et al., 2011). Most massive stars form in star clusters (e.g. Clarke et al., 2000; Lada & Lada, 2003), which are part of a hierarchical structure, defined by Williams et al. (2000) and summarized by Bergin & Tafalla (2007). In this approach, the largest structure is a molecular *cloud*, with masses of the order 10^3 - $10^4 M_\odot$ and diameters ranging from 2 to 15 pc. Clouds contain subunits of enhanced density gas and dust, called *clumps*, wherein the earliest stages of massive star formation take place. Clumps will typically form stellar clusters (Williams et al., 2000).

Studies of massive star formation regions showed that clumps generally have sizes of the order ~ 1 pc, and masses ranging from order $10 M_\odot$ to $\sim 10^3 - 10^4 M_\odot$ (Kurtz et al., 2000; Smith et al., 2009). They are defined to be coherent in position-velocity space. Smith et al. showed that the gravitational potential of these clumps causes global collapse, which channels mass from large radii towards the center of the cluster, where protostars with the greatest gravitational radius accrete it, causing them to become massive. Stars (or multiple systems such as binaries) eventually form from gravitationally bound sub-units in the clumps, called *cores* (Williams et al., 2000). Cores have sizes typically $\leqslant 0.1$ pc and masses ranging from $0.5 M_\odot$ up to $\sim 10^2 - 10^3 M_\odot$ (Kurtz et al., 2000; Smith et al., 2009).

We have corresponding $C^{18}O$ maps for 51 out of the 55 ^{13}CO maps. The optically thin $C^{18}O$ serves as a useful tracer of the central clump (e.g. López-Sepulcre et al., 2009). With a median source distance of 7.2 kpc and telescope beam of $14''$, our resolving power is of the order 0.5 pc, which, given the above definitions, implies the traced structures are more likely clumps than cores.

The $C^{18}O$ maps are used to calculate the H_2 clump masses. The $C^{18}O$ column density is calculated for each clump, again using equation 1 with $T_{trans} = 31.6$ K, T_{ex} unchanged, and T_{mb} the mean main-beam temperature for each clump's area, as derived from the intensity integrated image of each clump. The $C^{18}O$ column density of each clump is then converted to an H_2 column density using the Galactocentric distance dependant isotopic abundance ratio given by Wilson & Rood (1994) as $[C^{16}O]/[C^{18}O] = 58.8 D_{gal} + 37.1$, with the $[CO]/[H_2]$ ratio the same as described before. Finally the clump mass is calculated as

$$M_{clump} = (N_{H_2} \times A_{clump}) \, m_{H_2}, \qquad (11)$$

where A_{clump} is the surface area of each clump. These clump masses are listed in the last column of Table 6, and excluding sources with distance ambiguities, they have values ranging between 10 - 2200 $M_\odot$ with a mean of $\sim 420 M_\odot$ and median of $\sim 190 M_\odot$. The clump masses associated with the MMAO sub-set, have a mean of $\sim 460 M_\odot$.

However, López-Sepulcre et al. (2009) noted that their dust clump masses are a factor ~ 5 larger than the corresponding $C^{18}O$ masses, and stated that this difference might be explained by the fact that $C^{18}O$ and the sub-mm continuum are tracing different parts of the clump. They found

Table 6. Coordinates and masses of the central clumps associated with the methanol masers, as derived from the $870\mu m$ dust flux measurements from ATLASGAL (Csengeri et al., 2014). The last column lists the clump masses as calculated using $C^{18}O$ maps. (Suffixes "A" and "B" and numbers (1) and (2) next to some entries in column 1 have the same meaning as in Table 5).

Target	Clump coord. $l(°)$	$b(°)$	Dust flux S_ν (Jy)	$M_{870\mu m}$ $M_\odot$	$M_{C^{18}O}$ $M_\odot$
G 20.081-0.135	20.081	-0.135	10.5	9200	1800
G 21.882+0.013	21.875	0.008	3.7	65	20
G 22.038+0.222	22.040	0.223	5.5	430	41
G 22.356+0.066	22.356	0.068	5.4	810	64
G 22.435-0.169	22.435	-0.169	2.3	2300	200
G 23.003+0.124	23.002	0.126	0.9	200	18
G 23.010-0.411	23.008	-0.410	12.8	1700	110
G 23.206-0.378	23.209	-0.378	11.1	7100	370
G 23.365-0.291	23.364	-0.291	5.0	660	47
G 23.437-0.184	23.436	-0.183	11.9	2300	490
G 23.484+0.097	23.483	0.098	4.2	620	120
G 23.706-0.198	23.706	-0.197	3.9	2600	340
G 24.329+0.144	24.330	0.145	9.0	3000	91
G 24.493-0.039	24.493	-0.039	12.0	2700	300
G 24.790+0.083A	24.790	0.083	26.6	12000	670
G 24.850+0.087	24.853	0.085	2.4	530	240
G 25.650+1.050	25.649	1.051	16.6	14000	2200
G 25.710+0.044	25.719	0.051	0.6	300	250
G 25.826-0.178	25.824	-0.179	12.1	2100	120
G 28.148-0.004	28.148	-0.004	3.6	700	170
G 28.201-0.049	28.201	-0.049	15.7	7500	1800
G 28.282-0.359	28.289	-0.365	8.8	510	250
G 28.305-0.387	28.307	-0.387	4.3	2300	1200
G 28.321-0.011	28.321	-0.011	3.4	670	150
G 28.608+0.018	28.608	0.018	5.2	1600	680
G 28.832-0.253	28.832	-0.253	9.5	1500	130
G 29.603-0.625	29.600	-0.618	2.5	310	53
G 29.865-0.043	29.863	-0.045	4.2	1300	630
G 29.956-0.016A	29.956	-0.017	17.5	5200	900
G 29.956-0.016B	29.962	-0.008	3.5	1000	27
G 29.979-0.047	29.979	-0.048	6.5	1900	170
G 30.317+0.070	30.317	0.070	1.2	930	160
G 30.370+0.482A	30.370	0.484	1.2	1200	140
G 30.400-0.296	30.403	-0.296	1.9	570	120
G 30.419-0.232	30.420	-0.233	7.2	2100	290
G 30.424+0.466	30.424	0.464	1.9	1900	950
G 30.704-0.068	30.701	-0.067	22.0	3700	790
G 30.781+0.231	30.780	0.231	0.7	30	10
G 30.788+0.204	30.789	0.205	5.9	3000	320
G 30.819+0.273	30.818	0.273	1.8	380	53
G 30.898+0.162	30.899	0.163	3.7	1100	140
G 30.973+0.562(1)	30.972	0.561	0.7	660	150
G 30.973+0.562(2)	-	-	-	11	3
G 30.980+0.216	30.979	0.216	2.7	780	150
G 31.061+0.094(1)	31.060	0.092	1.0	930	130
G 31.061+0.094(2)	-	-	-	10	1
G 31.076+0.457(1)	31.085	0.468	1.5	1300	230
G 31.076+0.457(2)	-	-	-	34	6
G 31.122+0.063	31.124	0.063	0.9	700	290
G 31.182-0.148A	31.182	-0.148	1.1	830	too low S/N
G 31.282+0.062	31.281	0.063	13.1	3800	520
G 31.412+0.307	31.412	0.306	29.8	8700	1000
G 31.594-0.192(1)	31.593	-0.193	1.0	720	180
G 32.744-0.075	32.746	-0.076	7.8	6000	1100
G 33.317-0.360(1)	33.317	-0.360	0.6	500	too low S/N
G 33.317-0.360(2)	-	-	-	20	too low S/N
G 33.634-0.021	33.649	-0.024	2.3	630	190

the angular FWHM measured in the sub-mm continuum surveys to be a factor ~ 2.5 larger than what is mapped by $C^{18}O$ (J = 2-1), and speculated that this played a main role in the difference between the two mass estimates. Hofner et al. (2000) also concluded from their survey that masses derived from sub-mm dust emission, tend to be systematically higher than masses derived from $C^{18}O$ by a factor ~ 2. They pointed out that contributing sources of uncertainty to this discrepancy could be $C^{18}O$ abundance, optical depth estimates, and the dust grain emissivity adopted.

Therefore, we also use continuum measurements to calculate the clump masses associated with MMAOs, and use the latter in all further discussions. The 870 μm flux measurements were obtained from the ATLASGAL survey (Schuller et al., 2009; Contreras et al., 2013), using offsets within a FWHM beam (beam size 19″) as matching criteria. Using the matching fluxes from Csengeri et al. (2014) for the targets in this study, clump masses were calculated following Urquhart et al. (2013a), with a gas-to-dust mass ratio assumed to be 100, dust absorption coefficient κ_ν of 1.85 cm^2g^{-1} and dust temperature of 20 K. All values are listed in Table 6. Two clump masses are listed for sources with distance ambiguities, marked with (1) next to the name for the far distance, and (2) for the near distance. Excluding all targets with distance ambiguities, these clump masses range from $\sim 30 M_\odot$ to $1.4 \times 10^4 M_\odot$, have a mean value of $\sim (2.5 \pm 0.5) \times 10^3 M_\odot$ and median of $\sim 1.3 \times 10^3 M_\odot$. The clump masses associated with the MMAO sub-set, have a mean of $\sim 2.8 \times 10^3 \odot$. For the targets with resolved distances, 96% have masses $> 10^2 M_\odot$ and 49% have masses of the order $10^3 - 10^4 M_\odot$. This confirms that the majority of these targets are likely classified as clumps, as per definitions given above.

We find that the clump masses derived from dust measurements for our targets, are on average a factor 8 higher than masses derived using their $C^{18}O$ emission, in agreement with López-Sepulcre et al. (2009) and Hofner et al. (2000).

5   DISCUSSION

5.1   Clump and outflow mass relations

Here we investigate the relationships between outflow properties and the mass of the clumps that they are associated with. While it is not possible to resolve the contribution from individual stars or protostellar cores in our data we can at least infer a relationship between clump mass and the most massive star present in the clump (e.g. Urquhart et al., 2013b).

McKee & Tan (2003) derived a relation for the accretion rate of a free-falling envelope as a function of time, wherein it is proportional to the clump surface density $\Sigma^{0.75}$. This implies higher mass accretion in the most massive and dense clumps, compared to those forming in lower mass clumps. The former will arrive at the main-sequence sooner, and hence form an HII region much more quickly than less massive stars forming in lower-mass clumps. Urquhart et al. (2014) found their results to confirm this hypothesis, being consistent with the decreasing timescale with increasing massive YSO luminosity found by Mottram et al. (2011).

In addition to this, Urquhart et al. also found that the most massive stars form predominantly towards the centres of their spherical, centrally condensed host clumps, where the highest densities exists and the gravitational potential is the deepest. These stars evolve much quicker than those outside the central region, and reach the main sequence in $\sim 10^5$ yr, ahead of the lower-mass stars which can take ~ 10 times longer. Thus, while the most massive star, traced by the 6.7GHz methanol maser in this study, is near to joining the main sequence, it is likely that the lower-mass members of the proto-cluster still need to evolve to a stage where they make a significant contribution to the observed luminosity.

Urquhart et al. (2013b) found that for the HII regions they investigated, the bolometric luminosities (which are effectively a measure of the whole proto-cluster luminosity), were very similar to values estimated from the radio continuum flux (which only trace the most massive stars). This suggests that it is likely that the bolometric luminosity is actually dominated by the most massive stars. Urquhart et al. (2014) also found that there is a strong correlation between the clump masses and the bolometric luminosities of the most massive stars, but that the total clump luminosities are much lower than would be expected from the fully formed cluster. These findings agree with the stated hypothesis, that the most massive stars have very rapid evolution times, and are consequently likely to dominate the observed clump properties. Thus, if the luminosity of a clump is dominated by the most massive stars, then it is reasonable to assume that so too, is the luminosity, and consequently the energetics, of the outflow.

In the following, we compensate for the loss of one lobe's mass in monopolar targets by doubling the values of the detected lobe for M_{out}, p, E, $\dot{M}_{out}$, F_m and L_m, as they all depend on the outflow mass. Figure 5 (a) and (b) shows the relation between respectively outflow masses and mass loss rates, and clump masses for the MMAO sample (solid circles). In order to compare these relations with low-mass YSO's, we obtained associated outflow masses from Wu et al. (2004), Narayanan et al. (2012) and Davis et al. (2010) for 13 of the core envelope masses listed by Bontemps et al. (1996) (empty circles). The pink squares represent the clump masses from Beuther et al. (2002a), derived from 1.2 mm dust continuum data, together with their associated outflow masses and mass loss rates, as calculated in Beuther et al. (2002b). These values are corrected according to the erratum that was later published by Beuther et al. (2005), where the authors explain that their grain emissivity approximation should be a factor two higher than initially calculated, which would cause their derived clump masses to be a factor two lower than reported.

In Figure 5 (a), a best-fit power-law to the MMAO sample (circles) is given by $\log(M_{out}/M_\odot) = (-0.8 \pm 0.3) + (0.8 \pm 0.1)\log(M_{clump}/M_\odot)$, holding over three orders of magnitude for massive outflows, and extending toward the low mass regime to cover six orders of magnitude in total.

López-Sepulcre et al. (2009) converted their clump masses derived from $C^{18}O$ to dust masses, and found a tight correlation between M_{clump} and M_{out}, described by $M_{out} = 0.3 M^{0.8}_{clump}$. Sánchez-Monge et al. (2013) did a similar fit, but they calculated their outflow masses from SiO observations and clump masses from SED fits to Hi-GAL data. They found the same relation as López-Sepulcre et al. (2009). The power-law found for MMAOs agrees with
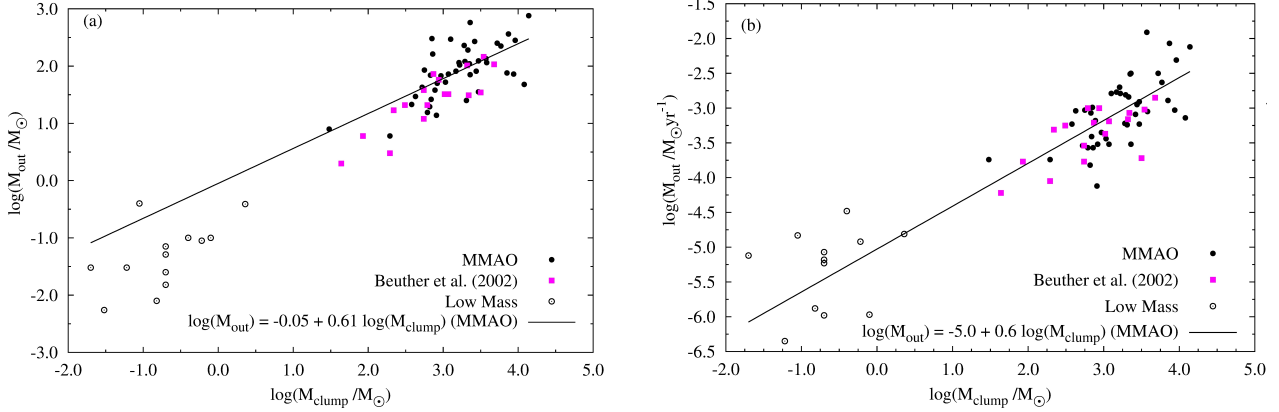
Figure 5. Relation between (a) outflow and clump masses and (b) outflow mass loss rate and clump masses, for MMAOs (solid circles), with the best-fit power laws shown. Empty circles indicate values for low mass YSOs, with core envelope masses from Bontemps et al. (1996) and associated outflow mass and mass loss rates from Wu et al. (2004), Narayanan et al. (2012) and Davis et al. (2010). Pink squares show the data from Beuther et al. (2002b).

these authors within uncertainties. It is interesting to note that the outflow masses and mass loss rates for MMAOs are generally higher than those estimated by Beuther et al. (2002b). We will discuss this property more detail in an upcoming second paper (de Villiers et al. 2014b in prep.).

Figure 5 (b) shows the best-fit linear relation between the logarithmic values for the mass loss rates and clump masses for MMAOs, given by $\log(\dot{M}_{out}/M_\odot yr^{-1}) = (-5.0 \pm 0.4) + (0.6 \pm 0.1)\log(M_{clump}/M_\odot)$. It again holds over three orders of magnitude for massive outflows, and extend to the low mass regime to cover six orders of magnitude in total.

As both M_{out} and $\dot{M}_{out}$ depend on mass and distance, a nonparametric measure of the statistical dependence between these parameters and M_{clump} is needed. The Spearman-rank test is used, similarly to Ridge & Moore (2001), where a perfect positive or negative correlation exists between the ranks when r_s is ± 1. No correlation exists when $r_s = 0$. The Spearman parameter r_s is related to the two-tailed Student's t-test via, $t_s = r_s\sqrt{(n-2)/(1-r_s^2)}$ for a sample size n. For no significant correlation, $|t_s| < |t_{s_{crit}}|$. For a sample size of 43 (MMAO sample of 44 had 43 matches from ATLAGAL for clump masses), $t_{s_{crit}}$ is ± 2.02. The relation between M_{out} and M_{clump} for MMAOs is statistically significant with $r_s = 0.59$ ($t_s = 4.66$). The same is true for the relation between $\dot{M}_{out}$ and M_{clump}, where $r_s = 0.64$ ($t_s = 5.28$).

The result that both relations in Figure 5 are found to hold over six orders of magnitude when extrapolated to the low-mass regime, suggests that a similar process causes outflows in both low and high mass star formation.

Figure 6 (a) shows the relation between the outflow mass and dynamical timescales for MMAOs. A power law fitted to the data resulted in a poor correlation given by $\log(M_{out}/M_\odot) = (0.3 \pm 1.2) + (0.3 \pm 0.3)\log(t/yr^{-1})$, with $r_s = 0.18$ ($t_s = 1.18$, for a complete MMAO sample of 44) implying no significant correlation, as also found by Wu et al. (2004). Our range of dynamical times is possibly too small for any significant evolutionary trends, such as the increase in outflow mass, to be observed.

Shepherd & Churchwell (1996a) plotted the same relation for their ten massive star forming regions. They divided their plot into three regions based on the bolometric luminosities of the outflow sources in Cabrit & Bertout (1992). We show the same luminosity boundaries in Figure 6 (a). Using data from Cabrit & Bertout (1992), Shepherd & Churchwell (1996a) found that sources with $L_* < 10^2 L_\odot$ were located below the bottom line and sources with $L_* > 2 \times 10^4 L_\odot$ above the top. This sectioning contributes a useful estimate of the expected bolometric luminosity of the YSO associated with each outflow studied - a property that could not be derived directly from the available data. Consistent with what is expected for massive YSO's, the majority (95%) of the sources occur above the $L_* = 10^2 L_\odot$ boundary, with $\sim 79\%$ of them between $L_* = 10^2 L_\odot$ and $L_* = 2 \times 10^4 L_\odot$, and $\sim 16\%$ above $L_* = 2 \times 10^4 L_\odot$. Also, we find that higher luminosity (and hence more massive) YSO's will drive the higher mass outflows we study in this paper. A more massive accreting YSO is likely to have higher angular momentum, hence power larger outflows. In addition to this, star formation regions that form O and B stars tend to have larger reservoirs of material available to be entrained into a molecular outflow.

Figure 6 (b) shows the relation between the CO momentum flux / mechanical force F_{CO} and the clump masses for MMAOs (circles), together with the values from Beuther et al. (2002b) (pink squares), as well as with 33 low mass sources from Bontemps et al. (1996) (triangles). F_{CO} is the inclination corrected mechanical force, derived from F_m by applying a correction factor of 2.9, corresponding to a mean inclination angle of 57.3^o (i.e. assuming random outflow orientations, Beuther et al. (2002b) and Table 4). Although we do not apply inclination corrections to the data in this study, in this specific case we correct F_m values in order to compare the CO momentum flux values from MMAOs with those from Beuther et al. (2002b) and Bontemps et al. (1996). Once again, as in Figure 5, MMAOs' momentum flux values are generally higher than those estimated by Beuther et al. (2002b) (also to be discussed by de Villiers et al., 2014b in prep.).

The outflow's mechanical force is a very important parameter in studying the early phases of star formation. It is a measure of the rate at which momentum is injected from the
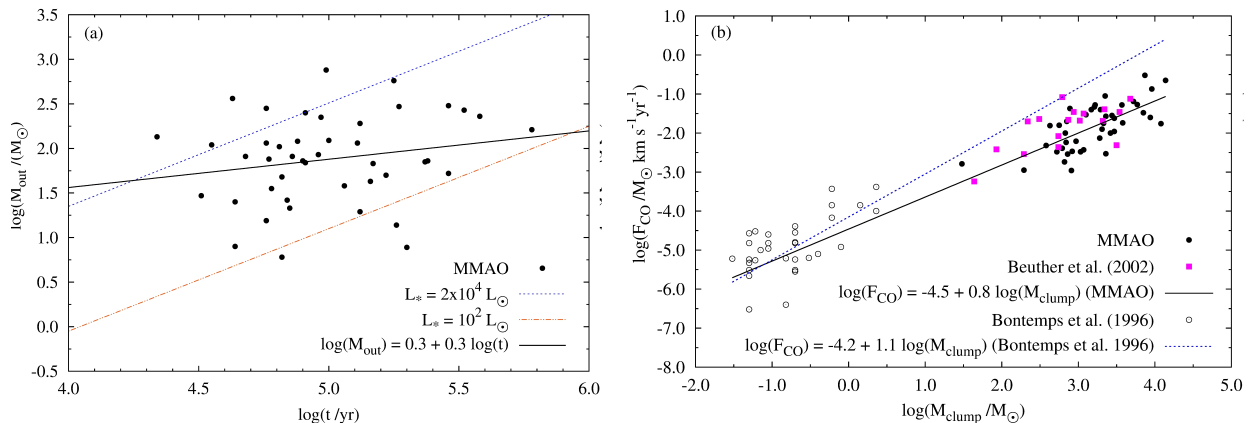
Figure 6. (a) Outflow masses versus dynamical time as derived from ^{13}CO for MMAOs, with the best-fit power law indicated by the solid line. Dot-dashed and dotted lines show respectively the lower and upper luminosity boundaries as defined by Shepherd & Churchwell (1996a). (b) Outflow mechanical force derived from ^{13}CO versus associated clump masses for MMAOs (solid circles). The solid line is a power-law fit to MMAOs and the dotted line the fit from Bontemps et al. (1996). Empty circles represent this relation for low mass YSOs (Bontemps et al., 1996), and pink squares show the data from Beuther et al. (2002b).

underlying driving agent, via interactions with the molecular gas in the core, into the envelope. In other words, it is a measure of the outflow's strength and used to understand the driving mechanism of outflows (Bachiller & Tafalla, 1999; Downes & Cabrit, 2007). Hatchell et al. (2007) suggests that, although it is difficult to separate this effect from contamination due to the initial conditions, the correlation between F_{CO} and M_{clump} suggests that the outflow activity declines during the later stages of the accretion phase (when the clump mass decreases).

Many authors have studied this relation before, both for low mass outflows (e.g. Bontemps et al., 1996; Hatchell et al., 2007; Takahashi et al., 2008; Curtis et al., 2010; van der Marel et al., 2013) and high mass outflows (e.g. Henning et al., 2000; Beuther et al., 2002b). For our massive MMAOs, we find the relation to be $\log\left(F_{CO}/M_\odot\mathrm{kms}^{-1}\mathrm{yr}^{-1}\right) = (-4.5 \pm 0.4) + (0.8 \pm 0.1)\log\left(M_{clump}/M_\odot\right)$ (black solid line) with a Spearman-rank coefficient of $r_s = 0.66(t_s = 5.62)$. This relation found for MMAOs corresponds within uncertainties to what Bontemps et al. (1996) found for low mass sources, $\log\left(F_{CO}/M_\odot\mathrm{kms}^{-1}\mathrm{yr}^{-1}\right) = -(4.2 \pm 0.1) + (1.1 \pm 0.2)\log\left(M_{clump}/M_\odot\right)$ (blue dotted line).

If, as stated in the beginning of this section, the outflow energetics are dominated by the most massive cores in a clump harbouring massive star formation, the presence of the same relationship between the outflow parameters and the clump masses for both high and low masses, is consistent with the theory that massive star formation is an scaled-up version of the low-mass scenario.

5.2 Mass loss rate and accretion rates

If massive outflows are produced by the same mechanism as low-mass outflows, it implies that the outflows are momentum driven by the jet coming from the central YSO which entrains the surrounding molecular gas and forms the outflow. One of the proposed solutions enabling disk accretion to be a possible formation process for massive stars, is when accretion proceeds through a disk with a high enough mass accretion rate to overcome the radiation pressure of

the central massive star (Jijina & Adams, 1996; Yorke & Sonnhalter, 2002). Even more involved disk accretion models including asymmetric configurations and Rayleigh-Taylor instabilities (Krumholz et al., 2007, 2009), assume accretion rates of the order 10^{-4} $M_\odot\mathrm{yr}^{-1}$. High accretion rates ($\sim 10^{-5} - 10^{-3}$ $M_\odot\mathrm{yr}^{-1}$) are also used in more recent disk accretion models that incorporate a dust sublimation front and consequently yielded the growth of the highest-mass stars ever formed in multi-dimensional radiation hydrodynamic simulations (Kuiper et al., 2010).

If one assumes that the momenta of the observed outflow and the jet entraining the outflow is conserved; (if there is efficient mixing at the jet/molecular gas interface and zero loss of momentum to the ISM Richer et al., 2000), Beuther et al. (2002b) stated that one could equate the momenta of the outflow and jet by

$$M_{out}\mathrm{v}_{out} = M_{jet}\mathrm{v}_{jet}. \tag{12}$$

Based on previous studies, they assumed that $v_{jet}/v_{out} \sim 20$. Using equation 12, one can write an expression for the jet mass loss rate as $\dot{M}_{jet} = M_{out}\mathrm{v}_{out}/\mathrm{v}_{jet}t_{dyn}$. Together with Beuther's assumption for jet and outflow velocity ratios, this mass loss rate from jets is described by $\dot{M}_{jet} = M_{out}\mathrm{v}_{out}/20$ $\mathrm{v}_{out}t_{dyn} = 0.05\dot{M}_{out}$. Furthermore, Beuther et al. (2002b) also assumed that $\dot{M}_{jet}/\dot{M}_{out_{accr}} \sim 0.3$ based on Tomisaka (1998); Shu et al. (1999), which leads to the following expression for accretion rate in terms of outflow mass loss rate:

$$\dot{M}_{out_{accr}} \sim \frac{\dot{M}_{out}}{6}. \tag{13}$$

The mean $\dot{M}_{out}$ for MMAOs is $\sim 1.7 \times 10^{-3}$ $M_\odot/\mathrm{yr}$, which would lead to accretion rates of $\sim 3 \times 10^{-4}$ $M_\odot/\mathrm{yr}$, being of the same order of magnitude as the $\sim 10^{-4}$ $M_\odot/\mathrm{yr}$ found by both Beuther et al. (2002b) and Kim & Kurtz (2006). Our approximate accretion rate for MMAOs is also much higher than typical accretion rates of $10^{-7} - 10^{-5}$ $M_\odot/\mathrm{yr}$ expected for low mass YSOs (Shu, 1977), and agrees with the theoretical rates used in disk
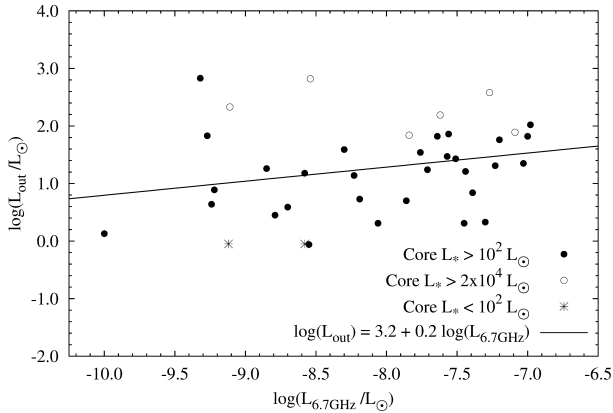
Figure 7. Outflow mechanical luminosities L_m derived from ^{13}CO plotted versus 6.7GHz Maser luminosities. The solid line indicates the best-fit power law to the data. Empty circles indicate sources located above the $2 \times 10^4 L_\odot$ bolometric luminosity boundary in Figure 6 (a), solid circles are sources located between the $L_* = 10^2 L_\odot$ and $L_* = 2 \times 10^4 L_\odot$ boundaries, and star symbols indicate sources located below $L_* = 10^2 L_\odot$.

accretion models for massive stars (Krumholz et al., 2007; Kuiper et al., 2010).

5.3 Comparison with Methanol masers

Integrated 6.7GHz flux densities (S_i) are obtained from the MMB catalogue (Breen et al. in prep., 2014) for 38 of the MMAO masers. Using the distance of each target, S_i is converted to an integrated spectral luminosity $L_{6.7\mathrm{GHz}}$.

Figure 7 shows the relation between the outflow mechanical luminosities (or energy supply rates) and maser luminosities for 38 masers from the MMAO sub-set, given as $\log(\mathrm{L_m/L_\odot}) = (3.2 \pm 1.3) + (0.2 \pm 0.2)\log(\mathrm{L_{6.7\mathrm{GHz}}/L_\odot})$ and a Spearman-Rank coefficient of $r_s = 0.28(t_s = 1.78)$, which, although not quite, is at the margin of being statistically significant as the 5% acceptance interval for t is ± 2.02.

Furthermore, following their positions in Figure 6 (a), we divide all the outflows plotted in Figure 7 into three categories; outflows associated with clumps whose luminosities above $2 \times 10^4 \mathrm{L_\odot}$, between the $L_* = 10^2 \mathrm{L_\odot}$ and $L_* = 2 \times 10^4 \mathrm{L_\odot}$, and below $L_* = 10^2 \mathrm{L_\odot}$. The data points in Figure 7 are marked accordingly. Although bright outflows are mostly associated with bright clumps, and low luminosity outflows associated with lower luminosity clumps, there is no such preference for maser brightness.

Finally we plot the relation between the 6.7GHz maser luminosities against clump masses in Figure 8 and found the best-fit linear relation between the logarithmic values of these parameters to be $\log(\mathrm{L_{6.7\mathrm{GHz}}/L_\odot}) = (-10.6 \pm 0.7) + (0.8 \pm 0.2)\log(\mathrm{M_{clump}/M_\odot})$. The associated value for r_s is 0.59 ($t_s = 4.36$), which implies a statistically significant positive correlation.

Breen et al. (2010) studied the relation between 101 1.2mm dust clumps and their associated 6.7GHz methanol masers. Their study showed that more luminous 6.7GHz methanol masers are likely to be associated with dust clump sources that have bigger radii, higher mass, and lower clump densities (the latter possibly due to the assumption of a
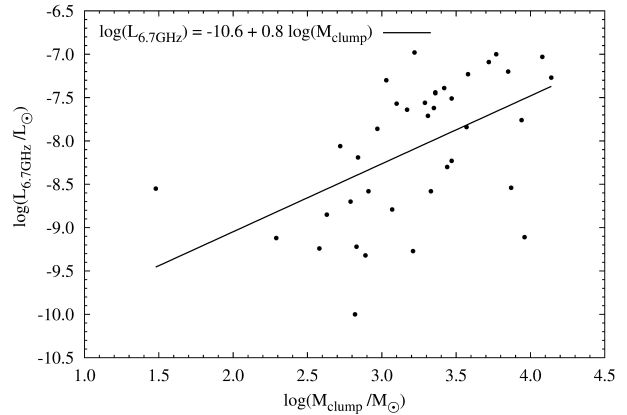

Figure 8. 6.7GHz Maser luminosities versus clump masses derived from 870 μm continuum emission.

constant dust temperature). These results are represented graphically in their Figure A2. Wu et al. (2010) also found molecular clumps (derived from NH_3 lines) associated with high-luminosity 6.7GHz masers to be larger and ~ 10 times more massive than those associated with low-luminosity masers. They also found that outflows associated with high-luminosity masers have wider line wings and larger sizes than those associated with low-luminosity masers. This lead to their interpretation that masers with higher luminosities are associated with YSO's with larger masses.

Urquhart et al. (2013a) found a weak linear correlation between the maser luminosity and clump masses for 442 ATLASGAL-MMB associations. They speculated that this correlation may be related to the fact that the most massive clumps are likely to form more massive stars, and that a higher isotropic maser luminosity is somehow related to a higher stellar luminosity.

The results from Figures 8 and 7 agrees with above authors and suggest that there is some correlation between the mass (hence also brightness) of a massive YSO and both the luminosity of the outflow it generates as well as the total 6.7GHz maser luminosity it pumps. Note that in this case, we know that a higher maser luminosity could not be due to a larger number of masers in more massive regions, as all our MMB-sample selected masers have supporting interferometric observations that reveal they are principally single maser spots.

6 SUMMARY AND CONCLUSIONS

We analysed the ^{13}CO and C^{18}O spectra extracted at 58 ^{13}CO clump coordinates toward 6.7GHz methanol maser coordinates between $20^o < l < 34^o$. All spectra showed high velocity outflow signatures. Of these, the high velocity emission was mapped for 55 with 47 showing bipolar structures. A sub-set containing 44 targets is referred to as MMAOs (Methanol Maser Associated Outflows), with the criteria that all members have to have resolved kinematic distances and be closely associated with a methanol maser. Only MMAOs were used for further analysis.

The wing spectra and spatial maps were used to calculate the physical properties of all 55 mapped outflows,

generally following Beuther et al. (2002b), with a few adjustments in their approach for this study. The associated clump masses for MMAOs were calculated from the 870 μm flux measurements towards these targets, of the ATLASGAL survey (Csengeri et al., 2014).

The main results for this study can be summarized as follows:

(i) A statistically significant relation over three orders of magnitude was found between the outflow and clump masses for the MMAOs, given by $\log(M_{out}/M_\odot) = (-0.8 \pm 0.3) + (0.8 \pm 0.1)\log(M_{clump}/M_\odot)$. This relation agreed, within uncertainties, with Beuther et al. (2002b), López-Sepulcre et al. (2009) and Sánchez-Monge et al. (2013). Low-mass sources (Bontemps et al., 1996; Wu et al., 2004; Narayanan et al., 2012; Davis et al., 2010) were found to follow a similar trend as the massive sources, expanding the power-law relationship to over six orders of magnitude.

(ii) The relation between the outflow mass loss rate and clump masses was described by $\log(\dot{M}_{out}/M_\odot yr^{-1}) = (-5.0 \pm 0.4) + (0.6 \pm 0.1)\log(M_{clump}/M_\odot)$, which held over six magnitudes down to the low-mass regime.

(iii) When plotting outflow masses against dynamical timescales, 95% of the MMAOs occurred above the $L_* = 10^2 L_\odot$ boundary for YSO luminosities, with $\sim 79\%$ of them between $L_* = 10^2 L_\odot$ and $L_* = 2 \times 10^4 L_\odot$, and $\sim 16\%$ above $L_* = 2 \times 10^4 L_\odot$. This suggests that higher luminosity (and hence more massive) YSOs will generate higher mass outflows.

(iv) The relationship between the mechanical force (CO momentum flux) F_{CO} and the clump masses was described by $\log\left(F_{CO}/M_\odot kms^{-1}yr^{-1}\right) = (-4.5 \pm 0.4) + (0.8 \pm 0.1)\log\left(M_{clump}/M_\odot\right)$, a trend which held over six orders of magnitude if we included low mass outflows.

(v) We derived an approximate accretion rate of $\sim 3 \times 10^{-4}$ $M_\odot$/yr from our mean mass loss rate. This is of the same order of magnitude than both the mean accretion rates found by Beuther et al. (2002b) and Kim & Kurtz (2006) and agrees with the theoretical rates used in disk accretion models for massive stars (Krumholz et al., 2007; Kuiper et al., 2010).

(vi) An investigation of the relation between the outflow mechanical luminosities and maser luminosities for 38 MMAO targets showed a weak positive correlation wherein bright outflows were associated with brighter masers and clumps. However, low luminosity outflows and clumps showed no preference for maser brightness. The relation between the 6.7GHz maser luminosities and clump masses was given by $\log(L_{6.7GHz}/L_\odot) = (-10.6 \pm 0.7) + (0.8 \pm 0.2)\log(M_{clump}/M_\odot)$. Although weakly correlated, these relations suggest that there is a correlation between the mass (hence also brightness) of a massive YSO and both the luminosity of the outflow it generates as well as the 6.7GHz maser it pumps. It agrees with the speculation from Urquhart et al. (2013a) that such a correlation may be related to the fact that the most massive clumps are likely to form more massive stars, and that a higher isotropic maser luminosity is somehow related to a higher stellar luminosity.

Results (i), (ii) and (vi) indicate that both the outflow mass relations and energetics follow a common relation for low- and high mass YSOs. This lends evidence to the hypothesis that a similar process is responsible for outflows in both mass regimes, i.e. high mass star formation is a scaled-up version of the low mass scenario. In addition to this, result (v) shows that the approximate mass accretion rate for MMAOs is sufficiently high to overcome the radiation pressure of a massive central star.

Although this evidence suggests that massive stars form in a similar fashion to low mass stars, to determine whether each massive YSO indeed drives it's own outflow, high resolution imaging is required.

In a following paper (de Villiers et al. 2014b in prep.), the outflow property distributions are compared to those from other surveys, focusing on the evolutionary sequence of 6.7GHz methanol masers and molecular outflows during the hot core phase.

7 ACKNOWLEDGEMENTS

REFERENCES

Arce, H. G., Borkin, M. A., Goodman, A. A., Pineda, J. E., & Halle, M. W. 2010, ApJ, 715, 1170

Bachiller, R. & Tafalla, M. 1999, in NATO ASIC Proc. 540: The Origin of Stars and Planetary Systems, ed. C. J. Lada & N. D. Kylafis, 227–+

Bally, J. & Zinnecker, H. 2005, AJ, 129, 2281

Bergin, E. A. & Tafalla, M. 2007, ARA&A, 45, 339

Beuther, H., Schilke, P., Menten, K. M., Motte, F., Sridharan, T. K., & Wyrowski, F. 2002a, ApJ, 566, 945

Beuther, H., Schilke, P., Menten, K. M., Motte, F., Sridharan, T. K., & Wyrowski, F. 2005, ApJ, 633, 535

Beuther, H., Schilke, P., Sridharan, T. K., Menten, K. M., Walmsley, C. M., & Wyrowski, F. 2002b, A&AS, 383, 892

Bonnell, I. A., Bate, M. R., & Zinnecker, H. 1998, MNRAS, 298, 93

Bonnell, I. A., Vine, S. G., & Bate, M. R. 2004, MNRAS, 349, 735

Bontemps, S., Andre, P., Terebey, S., & Cabrit, S. 1996, A&AS, 311, 858

Brand, J. & Blitz, L. 1993, A&AS, 275, 67

Breen, S. L., Ellingsen, S. P., Caswell, J. L., & Lewis, B. E. 2010, MNRAS, 401, 2219

Breen, S. L., Ellingsen, S. P., Contreras, Y., Green, J. A., Caswell, J. L., Stevens, J. B., Dawson, J. R., & Voronkov, M. A. 2013, MNRAS, 435, 524

Bronfman, L., Garay, G., Merello, M., Mardones, D., May, J., Brooks, K. J., Nyman, L.-Å., & Güsten, R. 2008, ApJ, 672, 391

Buckle, J. V., et al. 2010, MNRAS, 401, 204

Buckle, J. V., et al. 2009, MNRAS, 399, 1026

Cabrit, S. & Bertout, C. 1990, ApJ, 348, 530

Cabrit, S. & Bertout, C. 1992, A&AS, 261, 274

Cabrit, S., Goldsmith, P. F., & Snell, R. L. 1988, ApJ, 334, 196

Caswell, J. L. 2013, in IAU Symposium, Vol. 292, IAU Symposium, ed. T. Wong & J. Ott, 79–82

Caswell, J. L. & Green, J. A. 2011, MNRAS, 411, 2059

Cavanagh, B., Jenness, T., Economou, F., & Currie, M. J. 2008, Astronomische Nachrichten, 329, 295

Cesaroni, R., Galli, D., Lodato, G., Walmsley, C. M., & Zhang, Q. 2007, Protostars and Planets V, 197

Cesaroni, R., Walmsley, C. M., & Churchwell, E. 1992, A&AS, 256, 618

Chambers, E. T., Jackson, J. M., Rathborne, J. M., & Simon, R. 2009, ApJS, 181, 360

Chen, X., Ellingsen, S. P., & Shen, Z.-Q. 2009, MNRAS, 396, 1603

Chrysostomou, A., Bacciotti, F., Nisini, B., Ray, T. P., Eislöffel, J., Davis, C. J., & Takami, M. 2008, A&AS, 482, 575

Churchwell, E. 1999, in NATO ASIC Proc. 540: The Origin of Stars and Planetary Systems, ed. C. J. Lada & N. D. Kylafis, 515

Churchwell, E., et al. 2009, PASP, 121, 213

Clarke, C. J., Bonnell, I. A., & Hillenbrand, L. A. 2000, Protostars and Planets IV, 151

Clemens, D. P. 1985, ApJ, 295, 422

Codella, C., Lorenzani, A., Gallego, A. T., Cesaroni, R., & Moscadelli, L. 2004, A&AS, 417, 615

Codella, C. & Moscadelli, L. 2000, A&AS, 362, 723

Contreras, Y., et al. 2013, A&AS, 549, A45

Csengeri, T., et al. 2014, A&AS, 565, A75

Curtis, E. I., Richer, J. S., & Buckle, J. V. 2010, MNRAS, 401, 455

Cyganowski, C. J., Brogan, C. L., Hunter, T. R., & Churchwell, E. 2009, ApJ, 702, 1615

Cyganowski, C. J., et al. 2008, AJ, 136, 2391

Davis, C. J., et al. 2010, MNRAS, 405, 759

De Buizer, J. M., Bartkiewicz, A., & Szymczak, M. 2012, ApJ, 754, 149

De Buizer, J. M. & Vacca, W. D. 2010, AJ, 140, 196

Dent, W., et al. 2000, in Astronomical Society of the Pacific Conference Series, Vol. 217, Imaging at Radio through Submillimeter Wavelengths, ed. J. G. Mangum & S. J. E. Radford, 33

Downes, T. P. & Cabrit, S. 2007, A&AS, 471, 873

Dunham, M. K., Robitaille, T. P., Evans, II, N. J., Schlingman, W. M., Cyganowski, C. J., & Urquhart, J. 2011, ApJ, 731, 90

Ellingsen, S. P. 2006, ApJ, 638, 241

Fish, V. L., Reid, M. J., Argon, A. L., & Menten, K. M. 2003, ApJ, 596, 328

Frerking, M. A., Langer, W. D., & Wilson, R. W. 1982, ApJ, 262, 590

Garden, R. P., Hayashi, M., Hasegawa, T., Gatley, I., & Kaifu, N. 1991, ApJ, 374, 540

Goldsmith, P. F., Snell, R. L., Hemeon-Heyer, M., & Langer, W. D. 1984, ApJ, 286, 599

Gottschalk, M., Kothes, R., Matthews, H. E., Landecker, T. L., & Dent, W. R. F. 2012, A&AS, 541, A79

Green, J. A., et al. 2009, MNRAS, 392, 783

Green, J. A. & McClure-Griffiths, N. M. 2011, MNRAS, 417, 2500

Hatchell, J., Fuller, G. A., & Richer, J. S. 2007, A&AS, 472, 187

Hatchell, J., Thompson, M. A., Millar, T. J., & MacDonald, G. H. 1998, 133, 29

Henning, T., Schreyer, K., Launhardt, R., & Burkert, A. 2000, A&AS, 353, 211

Herbst, E. & van Dishoeck, E. F. 2009, ARA&A, 47, 427

Hofner, P., Wyrowski, F., Walmsley, C. M., & Churchwell, E. 2000, ApJ, 536, 393

Jijina, J. & Adams, F. C. 1996, ApJ, 462, 874

Kim, K.-T. & Kurtz, S. E. 2006, ApJ, 643, 978

Konigl, A. & Pudritz, R. E. 2000, Protostars and Planets IV, 759

Krumholz, M. R., Klein, R. I., & McKee, C. F. 2007, ApJ, 656, 959

Krumholz, M. R., Klein, R. I., McKee, C. F., Offner, S. S. R., & Cunningham, A. J. 2009, 323, 754

Kuiper, R., Klahr, H., Beuther, H., & Henning, T. 2010, ApJ, 722, 1556

Kurtz, S., Cesaroni, R., Churchwell, E., Hofner, P., & Walmsley, C. M. 2000, Protostars and Planets IV, 299

Lada, C. J. & Lada, E. A. 2003, ARA&A, 41, 57

López-Sepulcre, A., Codella, C., Cesaroni, R., Marcelino, N., & Walmsley, C. M. 2009, A&AS, 499, 811

McKee, C. F. & Tan, J. C. 2003, ApJ, 585, 850

Menten, K. M. 1991, ApJ, 380, L75

Minchin, N. R., White, G. J., & Padman, R. 1993, A&AS, 277, 595

Minier, V., Burton, M. G., Hill, T., Pestalozzi, M. R., Purcell, C. R., Garay, G., Walsh, A. J., & Longmore, S. 2005, A&AS, 429, 945

Minier, V., Conway, J. E., & Booth, R. S. 2001, A&AS, 369, 278

Minier, V., Ellingsen, S. P., Norris, R. P., & Booth, R. S. 2003, VizieR Online Data Catalog, 3403, 31095

Molinari, S., Brand, J., Cesaroni, R., & Palla, F. 1996, A&AS, 308, 573

Molinari, S., Brand, J., Cesaroni, R., Palla, F., & Palumbo, G. G. C. 1998, A&AS, 336, 339

Molinari, S., Testi, L., Rodríguez, L. F., & Zhang, Q. 2002, ApJ, 570, 758

Moore, T. J. T., Bretherton, D. E., Fujiyoshi, T., Ridge, N. A., Allsopp, J., Hoare, M. G., Lumsden, S. L., & Richer, J. S. 2007, MNRAS, 379, 663

Mottram, J. C., et al. 2011, ApJ, 730, L33

Narayanan, G., Snell, R., & Bemis, A. 2012, MNRAS, 425, 2641

Norberg, P. & Maeder, A. 2000, A&AS, 359, 1025

Ortega, M. E., Paron, S., Cichowolski, S., Rubio, M., & Dubner, G. 2012, A&AS, 546, A96

Parker, N. D., Padman, R., & Scott, P. F. 1991, MNRAS, 252, 442

Parsons, H., Thompson, M. A., Clark, J. S., & Chrysostomou, A. 2012, MNRAS, 424, 1658

Pestalozzi, M. R., Elitzur, M., & Conway, J. E. 2009, A&AS, 501, 999

Purcell, C. R., et al. 2006, MNRAS, 367, 553

Reid, M. J., et al. 2009, ApJ, 700, 137

Richer, J. S., Shepherd, D. S., Cabrit, S., Bachiller, R., & Churchwell, E. 2000, Protostars and Planets IV, 867

Ridge, N. A. & Moore, T. J. T. 2001, A&AS, 378, 495

Rodriguez, L. F., Carral, P., Ho, P. T. P., & Moran, J. M. 1982, ApJ, 260, 635

Roman-Duval, J., Jackson, J. M., Heyer, M., Johnson, A., Rathborne, J., Shah, R., & Simon, R. 2009, ApJ, 699, 1153

Sánchez-Monge, Á., López-Sepulcre, A., Cesaroni, R., Walmsley, C. M., Codella, C., Beltrán, M. T., Pestalozzi, M., & Molinari, S. 2013, A&AS, 557, A94

Schuller, F., et al. 2009, A&AS, 504, 415

Shepherd, D. S. & Churchwell, E. 1996a, ApJ, 472, 225

Shepherd, D. S. & Churchwell, E. 1996b, ApJ, 457, 267

Shu, F. H. 1977, ApJ, 214, 488

Shu, F. H., Allen, A., Shang, H., Ostriker, E. C., & Li, Z.-Y. 1999, in NATO ASIC Proc. 540: The Origin of Stars and Planetary Systems, ed. C. J. Lada & N. D. Kylafis, 193

Shu, F. H., Najita, J. R., Shang, H., & Li, Z.-Y. 2000, Protostars and Planets IV, 789

Shu, F. H., Ruden, S. P., Lada, C. J., & Lizano, S. 1991, ApJ, 370, L31

Simon, R., Rathborne, J. M., Shah, R. Y., Jackson, J. M., & Chambers, E. T. 2006, ApJ, 653, 1325

Smith, H., et al. 2008, in Society of Photo-Optical Instrumentation Engineers (SPIE) Conference Series, Vol. 7020, Society of Photo-Optical Instrumentation Engineers (SPIE) Conference Series

Smith, R. J., Longmore, S., & Bonnell, I. 2009, MNRAS, 400, 1775

Snell, R. L., Scoville, N. Z., Sanders, D. B., & Erickson, N. R. 1984, ApJ, 284, 176

Sobolev, A. M., Cragg, D. M., & Godfrey, P. D. 1997, A&AS, 324, 211

Sridharan, T. K., Beuther, H., Schilke, P., Menten, K. M., & Wyrowski, F. 2002, ApJ, 566, 931

Stahler, S. W. & Palla, F. 1993, in Bulletin of the American Astronomical Society, Vol. 25, American Astronomical Society Meeting Abstracts #182, 915

Su, Y.-N., Zhang, Q., & Lim, J. 2004, ApJ, 604, 258

Szymczak, M., Wolak, P., Bartkiewicz, A., & Borkowski, K. M. 2012, Astronomische Nachrichten, 333, 634

Takahashi, S., Saito, M., Ohashi, N., Kusakabe, N., Takakuwa, S., Shimajiri, Y., Tamura, M., & Kawabe, R. 2008, ApJ, 688, 344

Tomisaka, K. 1998, ApJ, 502, L163

Urquhart, J. S., et al. 2012, MNRAS, 420, 1656

Urquhart, J. S., et al. 2014, ArXiv e-prints

Urquhart, J. S., et al. 2011, MNRAS, 410, 1237

Urquhart, J. S., et al. 2013a, MNRAS, 431, 1752

Urquhart, J. S., et al. 2013b, MNRAS, 435, 400

van der Marel, N., Kristensen, L. E., Visser, R., Mottram, J. C., Yıldız, U. A., & van Dishoeck, E. F. 2013, A&AS, 556, A76

van der Walt, D. J., Sobolev, A. M., & Butner, H. 2007, A&AS, 464, 1015

van der Walt, J. 2005, MNRAS, 360, 153

Walsh, A. J., Macdonald, G. H., Alvey, N. D. S., Burton, M. G., & Lee, J.-K. 2003, A&AS, 410, 597

Williams, J. P., Blitz, L., & McKee, C. F. 2000, Protostars and Planets IV, 97

Williams, J. P., de Geus, E. J., & Blitz, L. 1994, ApJ, 428, 693

Wilson, T. L. & Rood, R. 1994, ARA&A, 32, 191

Wolfire, M. G. & Cassinelli, J. P. 1987, ApJ, 319, 850

Wu, Y., Wei, Y., Zhao, M., Shi, Y., Yu, W., Qin, S., & Huang, M. 2004, A&AS, 426, 503

Wu, Y., Yang, C., Li, Y., Lei, C., Sun, J., Lü, J., & Fu, H. 1999, Science in China A: Mathematics, 42, 732

Wu, Y. W., Xu, Y., Pandian, J. D., Yang, J., Henkel, C., Menten, K. M., & Zhang, S. B. 2010, ApJ, 720, 392

Xu, J.-L. & Wang, J.-J. 2013, Research in Astronomy and Astrophysics, 13, 39

Xu, Y., et al. 2006, AJ, 132, 20

Yorke, H. W. & Sonnhalter, C. 2002, ApJ, 569, 846

Zapata, L. A., Tang, Y.-W., & Leurini, S. 2010, ApJ, 725, 1091

Zhang, Q., Hunter, T. R., Brand, J., Sridharan, T. K., Cesaroni, R., Molinari, S., Wang, J., & Kramer, M. 2005, ApJ, 625, 864

Zhang, Q., Hunter, T. R., Brand, J., Sridharan, T. K., Molinari, S., Kramer, M. A., & Cesaroni, R. 2001, ApJ, 552, L167

Zinnecker, H. & Yorke, H. W. 2007, ARA&A, 45, 481